4/18/94
E8264
needs color

NASA
Contractor Report 4561

Army Research Laboratory
Contractor Report ARL–CR–109

Experimental Validation of Finite Element and Boundary Element Methods for Predicting Structural Vibration and Radiated Noise

A.F. Seybert, T.W. Wu, and X.F. Wu

GRANT NAG3–912
JANUARY 1994

NASA
National Aeronautics and
Space Administration

U.S. ARMY
ARL
RESEARCH LABORATORY

NASA
Contractor Report 4561

Army Research Laboratory
Contractor Report ARL–CR–109

Experimental Validation of Finite Element and Boundary Element Methods for Predicting Structural Vibration and Radiated Noise

A.F. Seybert, T.W. Wu, and X.F. Wu
University of Kentucky
Lexington, Kentucky

Prepared for
Propulsion Directorate
U.S. Army Aviation Systems Command
and
Lewis Research Center
Under Grant NAG3–912

Page intentionally left blank

TABLE OF CONTENTS

Page

Summary v

Chapter

1. INTRODUCTION 1

2. BOUNDARY ELEMENT METHOD 5

2.1 General 5

2.2 Formulation 6

2.2.1 The Linearized Wave Equation 6
2.2.2 Formulations for Free Space Problems 7
2.2.3 Formulation for Contact Problem 12
2.2.4 Numerical Implementation 14
2.2.5 Interpolation Technique Used in the BEM 18

3. ACOUSTICAL ANALYSIS OF GEAR HOUSING VIBRATION 20

3.1 Modal Analysis Experiments 20

3.2 Acoustical Analysis of Gear Housing Modes 20

3.2.1 Introduction 20
3.2.2 Sound Intensity and Sound Power 23
3.2.3 Sound Radiation Efficiency 23
3.2.4 The BEMAP Program 25

3.3 Results 25

3.3.1 Transmission Housing Modes 25
3.3.2 Sound Pressure and Sound Intensity Distributions 27
3.3.3 Radiation Efficiency 27

3.4 Structural Modification and Noise Control 36

3.5 Summary and Discussion 36

4. VALIDATION OF FEM/BEM PREDICTED STRUCTURAL VIBRATION AND RADIATED NOISE 41

4.1 Introduction 41

4.2 Sound Intensity Method 41

4.2.1 General 41
4.2.2 Modern Formulation for Intensity Measurement 42
4.2.3 Phase Calibration 44
4.2.4 The Sound Intensity Floor and Dynamic Range 45

4.3 Measurements....45

4.3.1 General.... 45
4.3.2 Vibration Measurements.... 45
4.3.3 Sound Intensity Measurements.... 48

4.4 FEM/BEM Models.... 48

4.4.1 Finite Element Model....48
4.4.2 Boundary Element Model.... 57

4.5 Results....62

4.6 Summary and Conclusions 69

5. THE EFFECT OF STIFFENING BY ADDING A RIB TO THE STRUCTURE.... 70

5.1 Introduction....70
5.2 FEM and BEM Models.... 70
5.3 Vibration.... 73
5.4 Radiation Efficiency and Total Radiated Sound Power.... 73
5.5 Discussion....82

6. SUMMARY, CONCLUSION AND SUGGESTION FOR FUTURE RESEARCH....88

REFERENCES....90

Summary

This research report is presented in three parts. In the first part, acoustical analyses were performed on modes of vibration of the housing of a transmission of a gear test rig developed by NASA. The modes of vibration of the transmission housing were measured using experimental modal analysis. The boundary element method (BEM) was used to calculate the sound pressure and sound intensity on the surface of the housing, and the radiation efficiency of each mode. The radiation efficiency of each of the transmission housing modes was then compared to theoretical results for a finite baffled plate.

In the second part, analytical and experimental validation of methods to predict structural vibration and radiated noise are presented. A rectangular box excited by a mechanical shaker was used as a vibrating structure. Combined finite element method (FEM) and boundary element method (BEM) models of the apparatus were used to predict the noise level radiated from the box. The FEM was used to predict the vibration, while the BEM was used to predict the sound intensity and total radiated sound power using surface vibration as the input data. Vibration predicted by the FEM model was validated by experimental modal analysis, noise predicted by the BEM was validated by measurements of sound intensity. Three types of results are presented for the total radiated sound power: (1) sound power predicted by the BEM model using vibration data measured on the surface of the box; (2) sound power predicted by the FEM/BEM model; and (3) sound power measured by an acoustic intensity scan.

In the third part, the structure used in part two was modified. A rib was attached to the top plate of the structure. The FEM and BEM were then used to predict structural vibration and radiated noise respectively. The predicted vibration and radiated noise were then validated through experimentation.

CHAPTER 1

INTRODUCTION

Helicopters have evolved into very versatile air mobile vehicles offering broad application for both military and civilian usage. Helicopter transmission research has progressed over two decades. One of the major goals of past research was to reduce noise and vibration, which are of concern for many reasons. Noise and vibration are not only aesthetically displeasing, they are also potentially dangerous to the pilot, crew, and passengers, as well as to the helicopter itself. The military is most concerned with pilot safety, workload, and efficiency, while commercial users are interested in attracting passengers who expect smooth and quiet riding with the convenience of taking off vertically from congested areas.

The interior noise of a helicopter ranges from 100-120 dB(A) [1]. The noise can come from many sources, such as the transmission, turbine engine compressor, exhaust system, rotor blades, and air turbulence. Through research, the National Aeronautics and Space Administration (NASA) and the helicopter industry have established that the transmission is the most prevalent source of noise [1, 2]. At least three sources of transmission noise have been identified: noise produced by gear teeth impacting when they engage; noise produced by air and oil displacing or pumping when the teeth engage; and noise radiated by the gear. The transmission path for impact-generated noise is structure borne; the energy passes through the gears, shafts and bearings and into the housing. The transmission path of the air-pumping noise is predominantly through the air inside the gear box. The path for gear-radiated noise is also the air inside the gear box [2].

NASA is currently studying the gear-impact noise problem [2]. Work is underway to determine and thus understand the path of transmission from the gears to the housing. However, very little work has been done to predict the noise that will be radiated by the housing. To date, little or no research appears to have been conducted to understand either the air-pumping noise or the noise radiated by the gears and their associated transmission path.

The air-pumping and gear-radiated noise couple to the gear housing through the air inside the gear box. The inside of the gear box is a sealed acoustical cavity, and as such, possesses acoustical resonances. Coupling between the gear-radiated noise and the housing will be most efficient when gear modes, cavity modes and gear housing modes lie in the same frequency band. Because all three resonant systems (gears, cavity and housing) have high modal density, it is likely that there are certain frequencies at which very efficient coupling occurs. The air-pumping noise also will couple to the housing through the resonant modes of the air cavity inside the gear box. From the gear housing to the helicopter cabin there are two primary paths by which noise will be transmitted: as noise radiated directly by the gear box and as vibration transmitted through the gear box mounted to the structural enclosure of the cabin.

The purpose of this research was to predict the extent of transmission of vibration and noise during the design stage and to validate both through experimentation. There are two steps involved in predicting noise radiated by a machine: the first is the determination of machine vibration, the second is the prediction of noise based on the predicted vibration or on the vibration obtained from other approaches (e.g., experimental data). The methods used to predict machine vibration include analytical methods and the finite element method (FEM), while methods used to predict machine-radiated noise include analytical methods, the finite element method, and the boundary element method (BEM).

Perreira and Dubowsky used a combined analytical-numerical method to model simply-shaped machine elements [3, 4]. In their work, a machine link was modeled as a vibrating beam in an infinite rigid baffle, and the Rayleigh integral was used to calculate the radiated noise. The major advantage of using the Rayleigh integral is its solution efficiency because the sound pressure can be obtained by direct integration of the known normal velocities. Certain simple machine elements may be modeled well by such treatments. However, the assumptions required in order to use the Rayleigh integral are rarely met by realistic vibrating structures.

The acoustic finite element method has been used successfully in predicting interior noise in machines and structures in which the acoustic field is calculated within an enclosed volume, such as printer enclosures and vehicle cabins. Small cavity enclosures treated with acoustical materials, sound sources, and apertures were modeled using the FEM by Bernhard and Takeo [5]. The sound pressure and sound intensity inside the cavity were predicted. The sensitivity of two acoustic design objective functions, the radiated sound power through apertures and the total energy in the cavity, to the surface acoustic treatments were also calculated. Sung and Nefske [6] used a coupled structural-acoustic finite element model to predict vibration and noise in vehicle cabins. The predicted structural response and sound pressure were verified by experiments. For exterior problems, however, the FEM encounters difficulties such as where to stop the domain discretization and requires enormous computational effort because a three-dimensional acoustic field must be discretized.

The boundary element method requires substantially less modeling and computational effort for exterior problems because only the boundary needs to be discretized, rather than the entire acoustic domain as with the FEM. Termination of domain discretization and attendant numerical closure, problems commonly encountered when using the domain methods, are not encountered when using the BEM. Another advantage of the BEM is that unknown variables on the surface are found directly without having to solve for the values at other points in the interior or the exterior region. Further, the unknown variables, whether interior or exterior to the domain of interest, may be found at any desired set of points using the BEM surface data.

Various researchers have verified the radiated noise predicted by the BEM by using spheres, cylinders, boxes, etc., where analytical solutions exist [7-9]. The prediction of noise using the BEM and the Rayleigh integral equation from measured vibration has also been verified by sound pressure measurements in a semi-anechoic chamber [10]. Oppenhiemer and Dubowsky used the FEM and the BEM to predict the sound power and sound pressure of a machine-like enclosure. The predicted sound power and sound pressure were then validated by experimentation. In their experiments, the sound pressure measurements were made in an anechoic room; the sound power measurements were conducted in a reverberant room. The sound power levels were computed from an average of sound pressure level measurements using the diffuse field idealization. Single frequency excitation was used for the acoustic measurements. Such excitations may not excite enough room modes to approximate a true diffuse field [11].

Another method used in acoustics is statistical energy analysis (SEA) [12, 13, 14]. The SEA may be applied to structural-acoustical problems. Using the SEA, a mechanical-acoustical system is divided into components such as plates, beams, and acoustic spaces. Linear energy balance equations that relate the average modal energy (energy per mode) contained within the components to the dynamic coupling between components are written and solved for the modal energy [12]. The modes of vibration that are of interest are those which correspond to the natural frequencies of the uncoupled sub-system which lie in the bandwidth under consideration. Response levels are related to modal energies, and power

flow is related to the coupling. This approach leads to a series of algebraic equations, the number of which depend upon the number of bandwidths in the frequency range of interest. For the SEA to provide an accurate representation of the system, the system must meet well-defined conditions. First, there must be several resonant modes in the frequency range of interest. Second, loose coupling must exist between the components. Third, the system must be divisible into components for which coupling and modal energy expressions are known.

The advantage of the SEA is its light computational burden. Systems are broken down into a few components rather than numerous finite or boundary elements. Also, the phase of the response does not need to be considered. Due to its simplicity, the SEA can also be used to indicate trends due to parameter variations. Cole, et al. used the SEA to study the noise reduction of an idealized cabin enclosure [14]. The attenuation, or noise reduction, of a rectangular steel box in a diffuse sound field was predicted using the SEA. Experimental measurements were performed in a reverberation chamber which was supplied with broadband white noise. The attenuation was measured in one-third octave bandwidths having center frequencies in the range of 63 Hz to 20 kHz. The results from the SEA agreed well with actual measured values.

While SEA has well-recognized advantage, the method also has its weaknesses. Systems with complex geometries or low modal densities do not meet the requirements of the SEA. Likewise, the SEA cannot predict exact temporal or spectral response. Since it is a statistical approach, the SEA works well at high frequencies, but is not accurate at low frequencies [14]. For low frequency applications the finite element and boundary element methods are more appropriate.

The conclusion drawn from this literature review was that the BEM is the best prediction tool to apply to problems having low to medium frequencies with responses composed of only a few modes. A BEM code BEMAP was used in this study. BEMAP calculates the pressure and sound intensity at field points in the near and far field of the sources, as well as sound pressure and sound intensity of the source itself. The sound intensity is integrated over the source to yield the sound power. While all of these quantities can be validated by measurements, some quantities are more accurate and suitable than others for experimental verification.

For example, sound pressure is a quantity that is dependent on the acoustic environment, and has no simple relationship to sound power, except under carefully controlled conditions based on special assumptions made about the sound field. When trying to quantify human response to sound, such as noise annoyance or the risk of hearing loss, sound pressure is the obvious quantity to measure. Sound intensity, which was used in the present study, however, has a simple relationship with sound power and can in principle be measured in any sound field. This property allows all the measurements to be conducted directly *in situ*, no expensive anechoic room or reverberant room is needed. Because the sound intensity is a vector with direction, it also can be used to locate the position of the noise sources.

The sound intensity method has previously been used in the research of helicopter transmission noise and vibration control. Atherton and Pintz [15] developed a Robotic Acoustic Intensity Measurement System (RAIMS) consisting of a two-channel spectrum analyzer (FFT), a desktop computer, an instrumentation robot arm, a digital control unit for the robot, and an acoustic intensity probe. This system was used to measure the sound field for different gears at various speeds and loads. It was found that gear tooth profile had a major effect on measured noise. Speed and load also have an effect on noise [15].

In the present research, a combined numerical and experimental validation of methods to predict structural vibration and radiated noise is presented. The modal superposition method was used to predict the vibration that was validated by experimental modal analysis. A modified Helmholtz integral equation for bodies sitting on an infinite plane [16] was used to predict the radiated noise which was validated by the sound intensity method. Three types of results are presented for the total radiated sound power: (1) sound power predicted by the BEM model using measured vibration data; (2) sound power predicted by the FEM/BEM model; and (3) sound power measured by the sound intensity method.

CHAPTER 2

BOUNDARY ELEMENT METHOD

2.1 General

The BEM is a numerical method used to solve a wide variety of boundary value problems. There are two approaches in the boundary element formulation: the direct boundary element method (DBEM) and the indirect boundary element method (IBEM). In the DBEM the problem is formulated in terms of the physical variables of interest, e.g., acoustical pressure and acoustical velocity. These variables are then solved directly from the discretized surface integral equations. In contrast, in the IBEM the problem is formulated in terms of a source density function, and a distribution of fictitious sources on the boundary is solved. Once the source solution on the boundary is known, the acoustic pressure or velocity at any boundary or field point can be determined. In the application of the BEM in acoustics, the DBEM corresponds to a numerical implementation of the Helmholtz integral equation [8, 9, 17-22], while the IBEM is a numerical implementation of Huygen's principle [23-25]. In this research, only the DBEM was used.

The mathematical formulation and practical application of the BEM are given in books by Brebbia [26], Brebbia and Walker [27], Brebbia, Telles and Wrobel [28], and the work of Banerjee and Butterfield [29]. The application of the BEM to wave problems can be found in Shaw's work [30]. Some overall reviews and applications of the BEM for the solution of acoustic problems [8, 17-19] governed by the Helmholtz equation for time-harmonic acoustic waves are available in the literature. All of these works utilized planar elements for the evaluation of the integral equation.

Recently, Seybert, et al [20-22], proposed an enhanced BEM for acoustic radiation and scattering problems with several improvements over the other work [8, 17-19]. These improvements include: the systematic handling of both smooth and nonsmooth (e.g., at an edge or a corner) geometries, the removal of the singularity in the Green function and its normal derivative, and the introduction of quadratic isoparametric elements to obtain the numerical solution of the Helmholtz integral equation.

One potential shortcoming of the BEM is that the exterior BEM formulation has the well-known difficulty of nonuniqueness of the solution at certain characteristic frequencies [30]. These fictitious eigenfrequencies have no physical meaning for the exterior boundary value problem being solved which has a unique solution for all frequencies. Schenck [9] has shown that uniqueness may be achieved by using the Combined Helmholtz Integral Equation Formulation (CHIEF) method. This method is to put additional points outside the acoustic domain to overdetermine the solution on the surface. The problem of nonuniqueness may also be treated analytically by forming a linear combination of the Helmholtz integral and its normal derivative [7, 31]. Seybert and Rengarajan [32] recently conducted a systematic study using the CHIEF method to overcome the nonuniqueness problem. The method was successfully tested for a variety of radiation problems with different geometries and boundary conditions at different frequencies.

The interior BEM formulation, however, does not suffer from the nonuniqueness problem described above for exterior problems. All eigenfrequencies for the interior problem are real and have a physical interpretation.

2.2 Formulation

2.2.1 The Linearized Wave Equation

Consider the propagation of small-amplitude acoustic waves in a stationary, inviscid, nonheat-conducting, homogeneous fluid medium. Let ρ_0, p_0 be the density and pressure of the fluid at rest, and denote the excess pressure and particle velocity at time t by p and u, respectively. From the linearized Euler's equation

$$\rho_0 \frac{\partial u}{\partial t} = -\nabla p, \tag{2.1}$$

and by the linearized continuity equation

$$\frac{\partial p}{\partial t} = -\rho_0 c^2 \nabla \cdot u, \tag{2.2}$$

where

$$c^2 = \gamma \frac{p_0}{\rho_0}, \tag{2.3}$$

in which c is the adiabatic speed of sound and γ is the ratio of the specific heats of the gas measured at constant pressure and constant volume. Equations (2.1) and (2.2) can be combined to yield a single differential equation

$$\nabla^2 p = \frac{1}{c^2} \frac{\partial^2 p}{\partial t^2}. \tag{2.4}$$

Equation 2.4 is the linearized, lossless wave equation for the propagation of sound in a fluid. If the acoustic quantities have a time harmonic behavior, $\exp(i\omega t)$, Eq. (2.4) reduces to the Helmholtz equation or the "reduced" wave equation

$$(\nabla^2 + k^2) p = 0, \tag{2.5}$$

where

$$k = \frac{\omega}{c} . \tag{2.6}$$

k is defined as the wave number and ω is the angular frequency.

It is usually appropriate to describe the sound field in terms of a scalar velocity potential which relates to the acoustic pressure and particle velocity through the relationships

$$p = i\omega\rho_0\phi \tag{2.7}$$

and

$$u = -\nabla\phi. \tag{2.8}$$

Therefore, the Helmholtz equation in terms of ϕ is

$$\nabla^2\phi + k^2\phi = 0. \tag{2.9}$$

2.2.2 Formulations for Free Space Problems

In principle, the boundary integral equation formulation for the wave equation can be derived from Green's second identity

$$\int_V (\psi \nabla^2\phi - \phi \nabla^2\psi) = \int_S (\psi \frac{\partial\phi}{\partial n} - \phi \frac{\partial\psi}{\partial n})dS, \tag{2.10}$$

in which ϕ and ψ are two sufficiently smooth scalar functions in V. The normal derivatives are defined as

$$\frac{\partial\phi}{\partial n} = \nabla\phi \cdot n \tag{2.11}$$

and

$$\frac{\partial \psi}{\partial n} = \nabla \psi \cdot n, \tag{2.12}$$

where n is the outward normal directed away from the region of interest, ϕ is the field variable (velocity potential for acoustic problems), and ψ is the fundamental solution determined from

$$\nabla^2 \psi + k^2 \psi = -4\pi\delta(P), \tag{2.13}$$

where $\delta(P)$ is the Dirac delta function at a point P. The solution of Eq. 2.13 is referred to as the free-space Green's function [33] and is given by

$$\psi = \frac{e^{-ikR}}{R}, \tag{2.14}$$

in which $R = |P - Q|$ is the distance between any spatial point Q and the singular point P.

The Interior Problem

Interior problems are governed by the Helmholtz equation where the acoustical region of interest, B, is enclosed by the surface, S, as shown in Fig. 2.1. Then,

$$\nabla^2 \phi + k^2 \phi = 0, \qquad \text{in B} \tag{2.15}$$

applying Green's second identity

$$\int_B (\psi \nabla^2 \phi - \phi \nabla^2 \psi)\, dV = \int_S \left(\psi \frac{\partial \phi}{\partial n} - \phi \frac{\partial \psi}{\partial n}\right) dS, \tag{2.16}$$

where n is away from the acoustic domain. The boundary integral representation of an interior problem is given by

$$C^0(P)\phi(P) = \int_S \left[\psi(P,Q) \frac{\partial \phi}{\partial n}(Q) - \frac{\partial \psi}{\partial n}(P,Q)\phi(Q)\right] dS(Q) \tag{2.17}$$

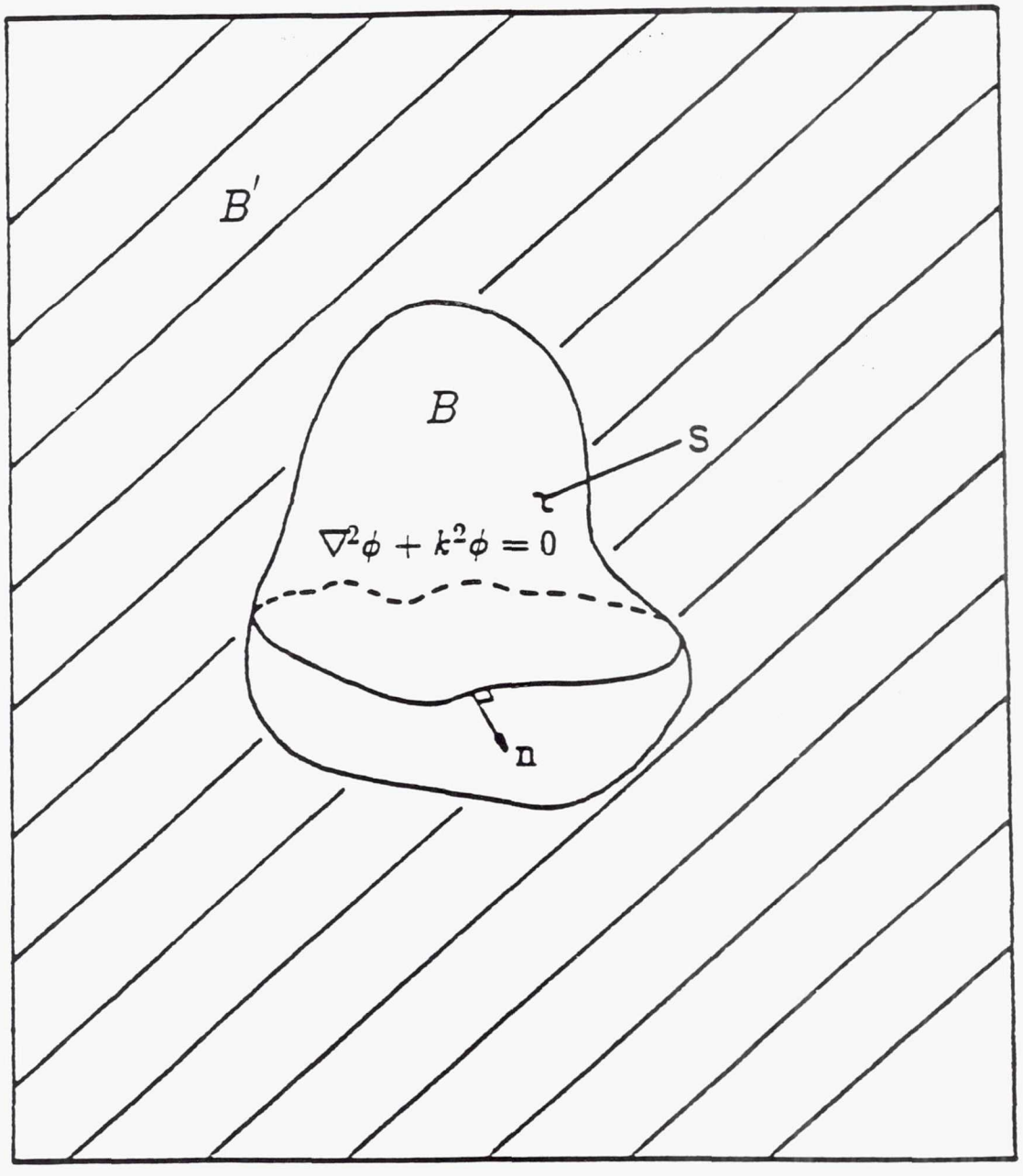

Figure 2.1 Schematic diagram of an interior acoustic problem .

where $C^0(P)$ is 4π for P in B, 2π for P in smooth S and 0 for P in B', and B' is the domain exterior to the surface, S. In general, $C^0(P)$ is a function of the local geometry at P on a nonsmooth surface, S, and can be evaluated by [34]

$$C^0(P) = -\int_S \frac{\partial}{\partial n}\left(\frac{1}{R}\right) dS. \tag{2.18}$$

The Exterior Problem

Exterior problems are governed by the Helmholtz equation where all the quantities are defined in B', which is outside of a given body, B, with surface, S, Fig. 2.2, i.e.,

$$\nabla^2\phi + k^2\phi = 0, \qquad \text{in B'} \tag{2.19}$$

Using Green's second identity

$$\int_{B'} (\psi \nabla^2\phi - \phi \nabla^2\psi)dV = \int_{S_\infty+S} (\psi \frac{\partial\phi}{\partial n} - \phi \frac{\partial\psi}{\partial n})dS, \tag{2.20}$$

and noting that

$$\int_{S_\infty} (\psi \frac{\partial\phi}{\partial n} - \phi \frac{\partial\psi}{\partial n}) dS = 0, \tag{2.21}$$

and using the Sommerfeld radiation condition [34], the boundary integral equation for an exterior problem is then reduced to

$$C(P)\,\phi(P) = \int_S [\psi(P,Q) \frac{\partial\phi}{\partial n}(Q) - \frac{\partial\psi}{\partial n}(P,Q)\phi(Q)]dS(Q), \tag{2.22}$$

where C(P) is 4π for P in B', 2π for p on smooth S and 0 for P in B. In general, C(P) can be evaluated by [34]

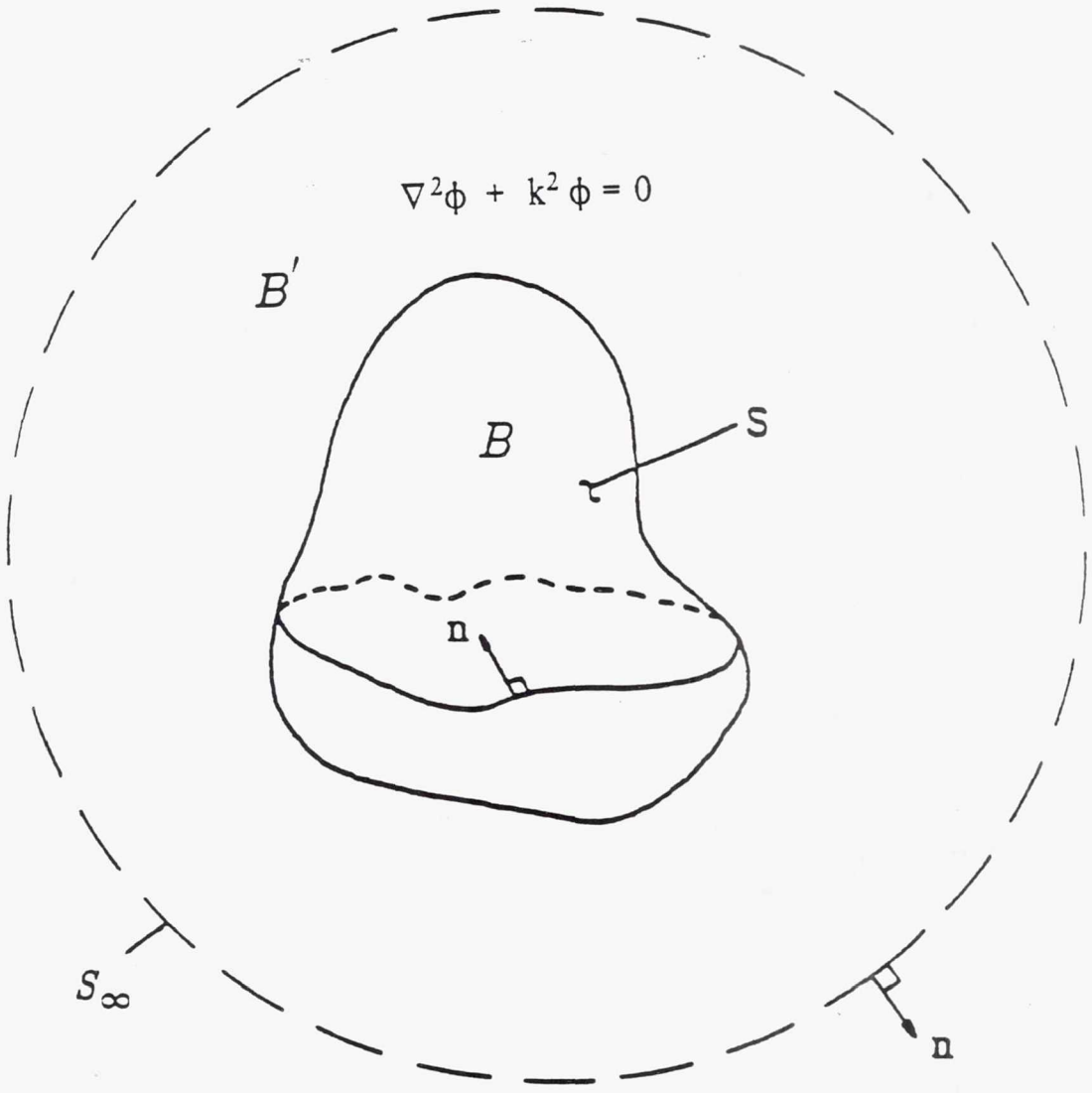

Figure 2.2 Schematic diagram of an exterior acoustic problem.

$$C(P) = 4\pi - \int_S \frac{\partial}{\partial n}(\frac{1}{R})dS, \qquad (2.23)$$

2.2.3 Formulation for Contact Problem

For a body sitting on a infinite plane (Fig. 2.3), the boundary of the body S can be divided into two parts. The first part is S_C, which is in contact with S_H; the other part is S_0, which is exposed to the acoustic medium B'. Then the boundary integral equation for acoustic radiation and scattering can be written as [16]:

$$C(P)\,\phi(P) = \int_{S_0} [\,\psi_H(P,Q)\ \frac{\partial\phi}{\partial n}(Q) - \frac{\partial\psi_H}{\partial n}(P,Q)\phi(Q)]dS(Q) + 4\pi\phi_I(P), \qquad (2.24)$$

where ϕ is the velocity potential satisfying the Helmholtz equation $\nabla^2\phi + k^2\phi = 0$ in B' and Sommerfeld radiation conditions in the far field, n is the inward normal, ϕ_I is the incident wave potential, and ψ_H is the half space Green's function, which takes the form:

$$\psi_H = e^{-ikr}/r + R_H(e^{-ikr_1}/r_1), \qquad (2.25)$$

R_H is the reflection coefficient of the infinite plane and r_1 is the distance between Q and the image point of P, with respect to S_H. The reflection coefficient R_H is equal to 1 for a rigid, infinite plane or -1 for a soft infinite plane. In the present study, the floor was considered rigid, thus $R_H = 1$.

The coefficient C(P) is still 4π for P in B', and zero for P in B. For P being on S_0 but not in contact with S_H, C(P) can be evaluated by [16]:

$$C(P) = 4\pi - \int_{S_0+S_C} \frac{\partial}{\partial n}(\frac{1}{r})dS. \qquad (2.26)$$

For P being on S_0, and also in contact with S_H, C(P) can be evaluated by [16]:

$$C(P) = (1+R_H)\,[\,2\pi - \int_{S_0+S_C} \frac{\partial}{\partial n}(\frac{1}{r})dS\,]. \qquad (2.27)$$

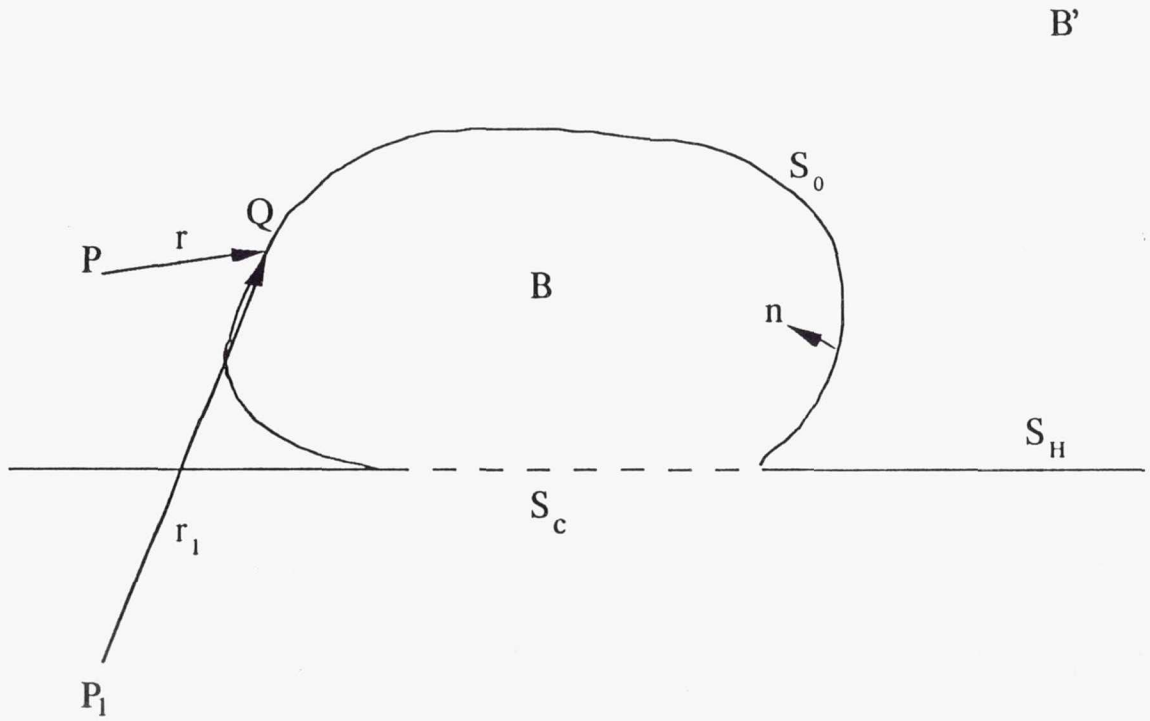

Figure 2.3 Nomenclature for a body sitting on a infinite plane.

2.2.4 Numerical Implementation

The numerical solution procedure for the BEM is divided into four steps. The first step is discretization of the boundary into boundary elements. The second step is numerical integration of the boundary integral equation to form a system of algebraic equations. The third step is the solution of the system of equations to obtain the unknown boundary values. The last step is the solution of the field values, if desired, by quadrature of the known values on the boundary.

In the standard BEM implementation, the boundary surface, S, is discretized into a number of elements and nodes. The number of elements were denoted by M and the number of nodes by N. If the singular point, P, is put at each of the N nodes alternately, N linear independent equations are obtained. Unlike the FDM or the FEM, in which the entire three-dimensional domain must be discretized, the BEM requires that only the boundary surface surrounding the body or cavity be discretized. If the domain is plane symmetric, only one-half of the surface has to be modeled. If the body is axisymmetric, a further simplification is achieved because the surface discretization can be accomplished with line elements [22]. In other words, only the generator of the body or cavity needs to be discretized.

In the classical BEM, the surface is discretized into a number of planar surface elements, and the acoustical variables, ϕ and ϕ', are assumed constant on each element. This piecewise constant approximation has been used with good results [19, 24]. But a very fine mesh may be required to obtain an adequate representation for ϕ and ϕ'. Recently, the BEM has been improved by the use of quadratic isoparametric elements [20-22] in which quadratic shape functions are used to represent both the geometry and the acoustic variables within each element. The discretization scheme used herein involves quadratic isoparametric surface elements of either quadrilateral or triangular shape for a three- dimensional body or cavity (Fig. 2.4(a)). The quadratic shape functions allow the use of fewer elements to approximate a curvature surface. At the same time, they also give more accurate approximation for the geometry and the acoustic variables. For a body or cavity which is axisymmetric, the generator of the body or cavity may be simply modeled by three-node isoparametric line elements [22, 35].

The global Cartesian coordinates X_i (i =1, 2, 3) of any points of an element are assumed to be related to the nodal coordinates, $X_{i\alpha}$, by

$$X_i(\xi) = \sum_{\alpha} N_\alpha(\xi)\, X_{i\alpha}, \qquad \alpha = 1, 2, \ldots, 6 \text{ or } 8 \tag{2.28}$$

in which $N_\alpha(x)$ are second order shape functions of the local coordinates $(\xi) = (\xi_1, \xi_2)$ $(-1 \le 1\xi \le 1)$, Figure 2.4(b). Equation (2.28) is an implicit transformation in which a surface element is mapped into a plane square or a plane equilateral triangle.

Next, the same quadratic shape functions were used to interpolate the boundary variables ϕ and ϕ' ($\equiv \frac{\partial \phi}{\partial n}$). On each element, it was assumed

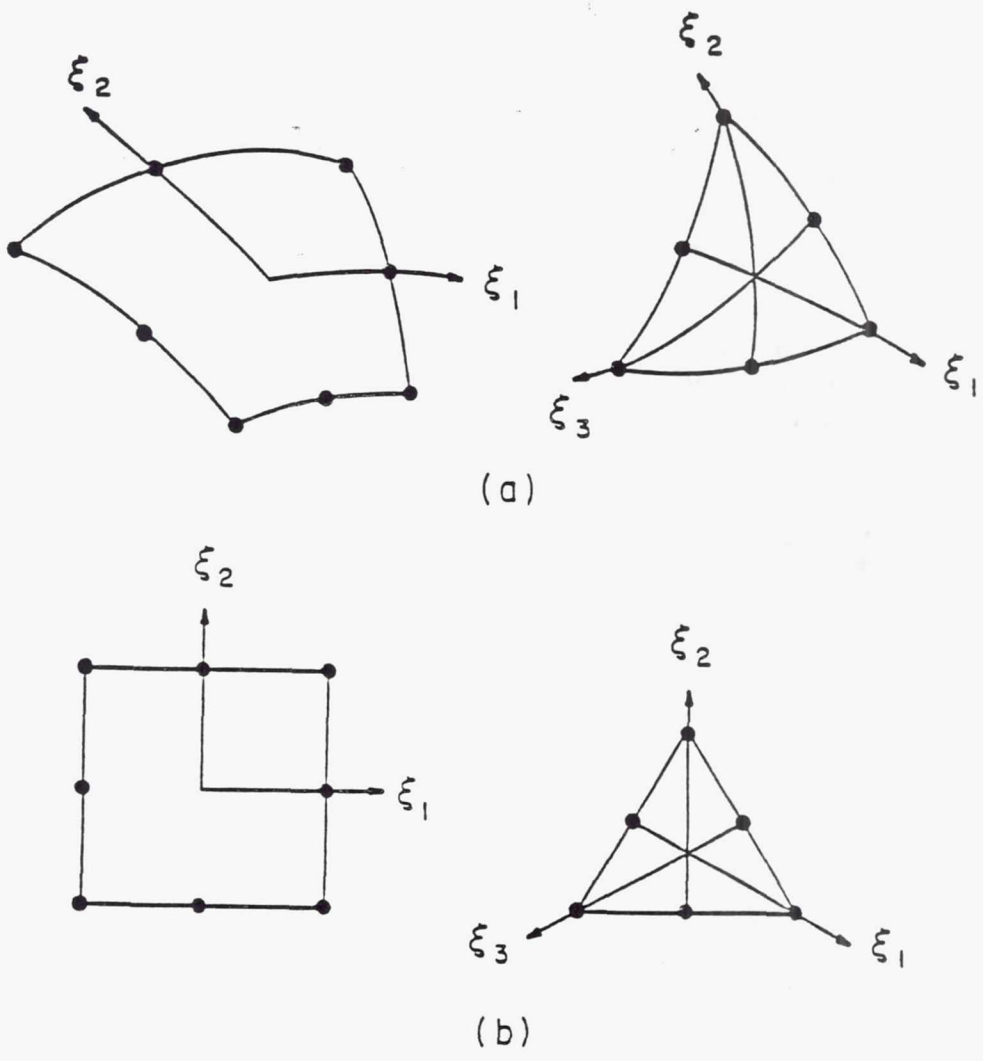

Figure 2.4 (a) Curvilinear quadrilateral and triangular elements.
(b) Corresponding parent elements .

$$\phi_m(\xi) = \sum_{\alpha} N_\alpha(\xi)\, \phi_{m\alpha}, \tag{2.29}$$

and

$$\phi'_m(\xi) = \sum_{\alpha} N_\alpha(\xi)\, \phi'_{m\alpha}, \tag{2.30}$$

where $\phi_{m\alpha}$ and $\phi_{m\alpha}$' are the nodal value of ϕ and ϕ', respectively. For an interior problem, evaluating Eq. (2.17) over the discretized surface S, substituting equations (2.28) - (2.30) into equation (2.17) for each point P and element S_m combination, we obtain

$$\sum_m \sum_\alpha a_{mj}^{\alpha}\, \phi_{m\alpha} - \sum_m c_{mj}\, \phi_j = \sum_m \sum_\alpha b_{mj}^{\alpha}\, \phi'_{m\alpha}, \tag{2.31}$$

where

$$a_{mj} = \int_{S_m} \frac{\partial \psi}{\partial n} N_\alpha(\xi)\, J(\xi) d\xi, \tag{2.32}$$

$$b_{mj} = \int_{S_m} \psi N_\alpha(\xi)\, J(\xi) d\xi, \tag{2.33}$$

and

$$c_{mj} = \int_{S_m} \frac{\partial}{\partial n} \left(\frac{1}{R_j(\xi)} \right) J(\xi) d\xi, \tag{2.34}$$

where α = 1, 2, ..., 6 or 8, j is a global node number and $R_j(\xi)$ is the distance from node j to every point, Q, on element m. S_m is the area of the mth element and $J(\xi)$ is the Jacobian of the isoparametic transformation

$$J(\xi) = \left| \frac{\partial \mathbf{x}}{\partial \xi_1} \times \frac{\partial \mathbf{x}}{\partial \xi_2} \right|, \tag{2.35}$$

where $\mathbf{x}$ is the position vector of the point Q. The unit normal to the surface, S, can be evaluated as

$$n = \frac{\dfrac{\partial \mathbf{x}}{\partial \xi_1} \times \dfrac{\partial \mathbf{x}}{\partial \xi_2}}{J(\xi)}. \tag{2.36}$$

Hence, whether the surface is axisymmetric or fully three-dimensional, for a total number of nodes, N, a system of N simultaneous algebraic equations in terms of the unknown, ϕ and ϕ', is produced. Eq. (2.31) then can be written in matrix form

$$[A]\ \{\phi\} = [B]\ \{\phi'\}, \tag{2.37}$$

where the elements in matrices A and B are obtained by collecting terms from Eq. (2.31). For a well-posed boundary value problem, either ϕ or ϕ' is known on the boundary, the matrix form can be reduced to

$$[K]\ \{a\} = \{f\}, \tag{2.38}$$

where [K] is a N×N square, fully populated, nonsymmetric matrix of boundary element coefficient, {a} is the unknown vector (either $\{\phi\}$ or $\{\phi'\}$) and {f} is the known vector on the boundary. The unknowns on the boundary can be found by solving Eq. (2.38), and the field point velocity potential can then be found by using Gaussian quadrature.

For numerical implementation of the exterior problem given by Eq. (2.22), using the same procedure as for the interior problem can yield

$$\sum_m \sum_\alpha a^{\alpha}_{mj} \phi_{m\alpha} + [\, 4\pi - \sum_m c_{mj} \,] \phi_j = \sum_m \sum_\alpha b^{\alpha}_{mj} \phi'_{m\alpha}. \tag{2.39}$$

Note that the normal used to evaluate a, b, and c in equations (2.32) to (2.34) is opposite to that for an interior problem.

In order to obtain an accurate BEM solution, the elements of the coefficient matrices [A] and [B] in Eq. (2.37) must be evaluated accurately. These calculations include the evaluation of Eqs. (2.32) to (2.34) by an appropriate numerical integration scheme. The accuracy of these calculations depends on the number and size of the elements and the type of integration and the number of integration points used. The determination of the elements of the coefficient matrices [A] and [B] involves the evaluation of integrals of the type [34]

$$I_{mj} = \int_{S_m} N_\alpha(\xi)\, K_{mj}(P_j, Q(\xi))\, J(\xi)\, d\xi, \qquad (2.40)$$

where P_j is a boundary node at which the integral is evaluated, $Q(\xi)$ is the variable boundary point, and $K_{mj}(P_j, Q(\xi))$ is the kernel function, either ψ or ψ'. Apparently K_{mj} has a singularity (i.e., $1/R$ for ψ, $1/R^2$ for ψ') when $R_j(\xi)=0$, which will occur when $P_j \in S_m$. Therefore, special care must be taken to remove such singularity. In general, evaluation of equation (2.40) may have two cases. In the first case, $P_j \notin S_m$, i.e., point P_j is not on the element under consideration. Therefore, the integral is nonsingular. Eq. (2.40) can be evaluated using a standard Gaussian quadrature formulation.

For the second case, $P_j \in S_m$, i.e., the point P_j is on the element under consideration. The removal of the $1/R$ and $1/R^2$ singularities can be achieved by performing the polar coordinate transformation [34]. By changing to a local polar coordinate system (R, θ), in which the origin is selected at the point where the singularity occurs, the element of area dS becomes $RdRd\theta$. For $K_{mj}(P_j, Q(\xi)) \propto O(1/R)$, it is obvious that the singularity is removed because the extra factor, R, produced by the polar coordinate transformation (the 'O' means that the convergence is of the order contained in the parenthesis). For $K_{mj}(P_j, Q(\xi)) = \psi'$, note that $K_{mj}(P_j, Q(\xi))$ is $O(1/R^2) \cdot \partial R/\partial n$, or $K_{mj}(P_j, Q(\xi)) \propto O(1/R)$ since $\partial R/\partial n$ is O(R). Again, this singularity is removed. Hence, the integral in Eq. (2.40) can be calculated using the regular Gaussian quadrature in both R and θ directions.

2.2.5 Interpolation Technique Used in the BEM

Although the BEM is a very efficient numerical technique for acoustic analysis for a single frequency, it may lose its advantage for a multifrequency run. The main reason is that the integrals in Eqs. (2.32) and (2.33) are frequency dependent. For each different frequency, all the components in the coefficient matrix [K] and the right hand side vector {f} need to be re-calculated. The procedure will be very time consuming if solutions over a wide frequency spectrum are required.

Recently, a frequency interpolation technique has been proposed by Schenck and Benthien [36] for multifrequency analysis in their acoustic BEM code. Only constant elements are used in Ref. [36]. The concept was expanded to isoparametric elements in the BEM code used in the present study [37]. It can be seen from Eqs. (2.32) and (2.33) that both a_{mj} and b_{mj} may vary rapidly with frequency due to the kernel e^{-ikr}. The rapid variation with frequency can be smoothed out by premultiplying Eqs. (2.32) and (2.33) by a factor, $e^{ik\bar{r}}$, that is

$$\bar{a}_{mj} = e^{ik\bar{r}} \int_{S_m} \frac{\partial \psi}{\partial n} N_\alpha(\xi)\, J(\xi) d\xi, \qquad (2.41)$$

and

$$\bar{b}_{mj} = e^{ik\bar{r}} \int_{S_m} \psi N_\alpha(\xi) J(\xi) d\xi, \tag{2.42}$$

where $\bar{r}$ is the distance between P and the centroid of the element, S_m. Then, linear interpolation between two reasonably spaced frequencies can be performed on the basis of $\bar{a}_{mj}$ and $\bar{b}_{mj}$. After we obtain the $\bar{a}_{mj}$ and $\bar{b}_{mj}$ vectors at a new frequency through interpolation, the a_{mj} and b_{mj} vectors at that frequency can be obtained immediately by

$$a_{mj} = e^{-ik\bar{r}} \bar{a}_{mj}, \tag{2.43}$$

and

$$b_{mj} = e^{-ik\bar{r}} \bar{b}_{mj}, \tag{2.44}$$

where the operation is simply the inverse transformation of Eqs. (2.41) and (2.42).

CHAPTER 3

ACOUSTICAL ANALYSIS OF GEAR HOUSING VIBRATION

As discussed in Chapter 1, transmission noise is an important component in the total noise radiated into the cabin of a helicopter. Transmission noise reaches the cabin by two primary paths: a structural path by which vibrational energy is transmitted through transmission mounts and load-carrying members to the cabin walls, and a direct radiation path in which sound radiated from the transmission excites the cabin wall or passes into the cabin through openings. The relative importance of these paths depends on the specific design of the helicopter and the location of the transmission.

In this part of the present research, the direct radiation of sound from the transmission was of interest. Sound radiated by the transmission is a function of the forces applied to the transmission, the structural properties of the transmission, and the radiation efficiency of the transmission. The vibration response of the transmission may be described by a superposition of the modes of vibration of the transmission. It is, therefore, important to know the modes of vibration and the radiation efficiency of these modes. In this study, the vibrational modes of the transmission were measured using experimental modal analysis. The boundary element method (BEM) was used to calculate the acoustic field produced by each mode of vibration. The BEM is used to calculate the sound pressure and sound intensity distributions on the surface of the transmission, the far field sound pressure directivity of each mode, and the relative sound power and sound radiation efficiency of each mode of vibration of the transmission.

3.1 Modal Analysis Experiments

As a means of understanding the relationship between noise and gear design parameters, NASA Lewis Research Center developed a gear noise test rig, as shown in Fig. 3.1(a). The detail of the gearbox was shown in Fig. 3.1(b). In the present study, the gearbox was analyzed using experimental modal analysis to determine the modes and natural frequencies of the gear housing [38]. Eight modes were found in the frequency range 650-3000 Hz. Two of the gear housing modes are shown in Figs. 3.2 and 3.3. Because the top of the gear housing is not as stiff as the sides, most of the modes resemble classic plate modes of the top surface. The mode in Fig. 3.2, for example, looks very much like a 1,1 plate mode, while the mode in Fig. 3.3 is similar to a 4,1 mode. All but one of the modes (occuring at 2000 Hz) exhibited dominant plate modes of the top surface.

3.2 Acoustical Analysis of Gear Housing Modes

3.2.1 Introduction

The BEM was used to analyze the acoustical properties of the modes of vibration of the gear housing. The BEM has been used previously to analyze the modes of vibration of engines [39, 40], to model the sound fields inside of vehicles and aircraft, and to predict the performance of mufflers and silencers [41, 42].

As discussed earlier, the BEM is based on the Helmholtz integral equation

$$C(P)\phi(P) = \int_S [\psi(P,Q)\frac{\partial\phi}{\partial n}(Q) - \frac{\partial\psi}{\partial n}(P,Q)\phi(Q)]dS(Q), \qquad (3.1)$$

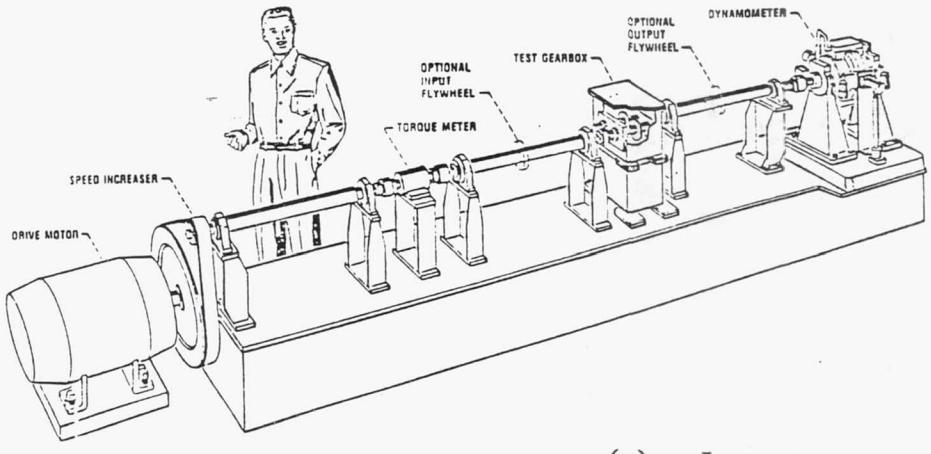

(a). Layout

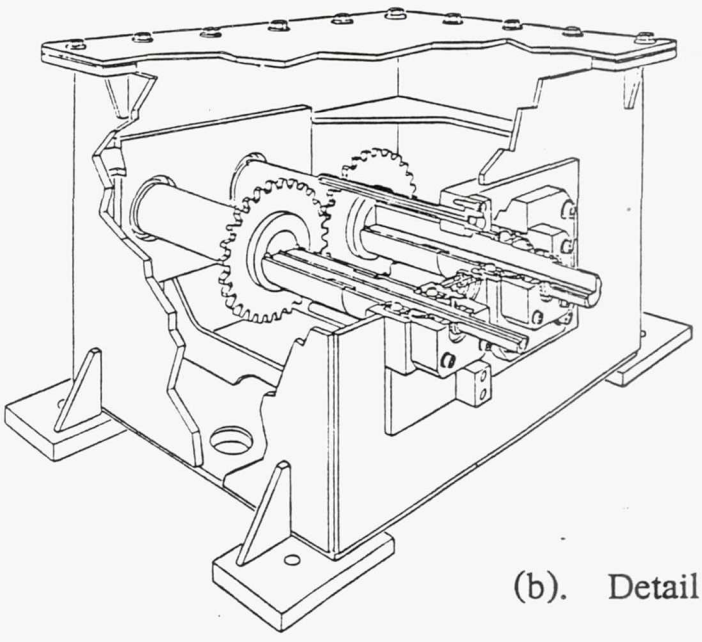

(b). Detail of gearbox

Figure 3.1 NASA gear noise rig

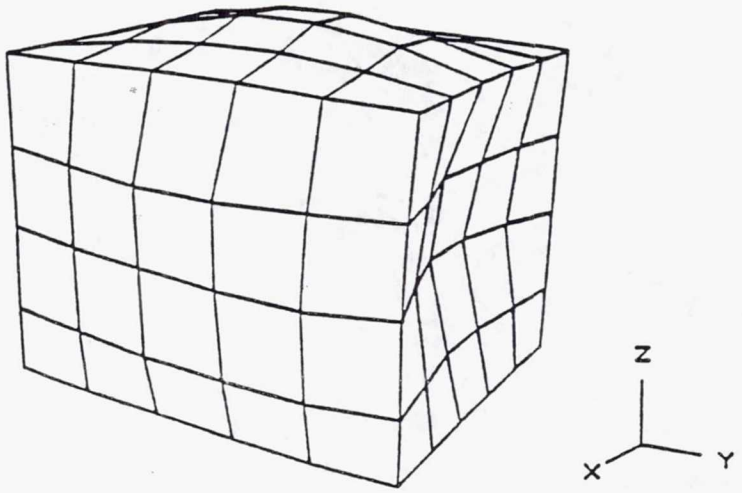

Figure 3.2 658 Hz mode of the transmission housing.

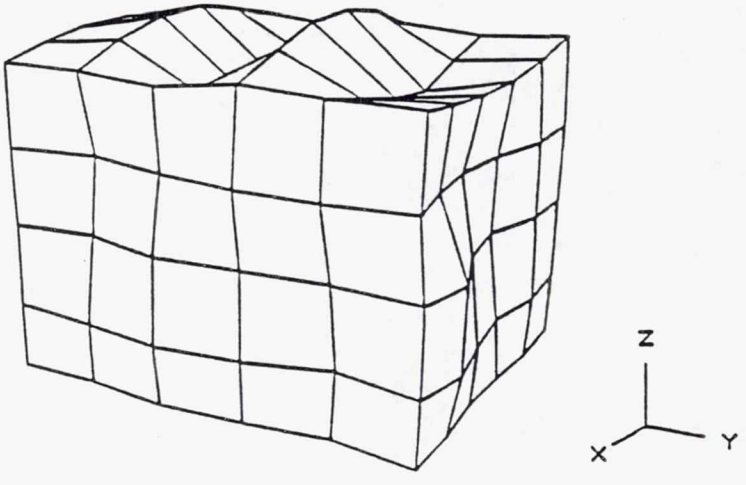

Figure 3.3 2722 Hz mode of the transmission housing.

where C(P) is 4π for P in the field around the housing and is 2π for P on the surface, S, of the housing. The Helmholtz integral equation is used to determine the ϕ at any point, P (see Fig. 3.4) in the acoustic medium surrounding the gear housing or on the housing itself as a function of the normal velocity of vibration v of the housing.

Equation (3.1) states that the velocity potential, ϕ (or pressure p), at a point in the acoustic medium may be found by summing up (integrating) two terms over the entire surface S of the housing, one involving the vibration velocity v on the surface of the housing and the other involving the velocity potential ϕ (or pressure p), on the surface of the housing. However, the pressure on the surface of the housing is not known initially and must be determined from solving Eq. (3.1) by considering point P on the surface S. Once this is done, Eq. (3.1) may be used to determine the pressure at any point in the medium.

3.2.2 Sound Intensity and Sound Power

Once both {v} and {p} are known on the surface S (i.e., at every node), the pressure at any point in the near field or far field may be determined from a discretized form of Eq. (3.1). Further, the sound intensity I at every point Q on the surface may be calculated from

$$I(Q) = \mathrm{Re}\{p(Q)\, v^{*}(Q)\}/2, \tag{3.2}$$

where Re denotes the real part of the expression in parentheses and * denotes the complex conjugate. Intensity is the sound power radiated per unit area of the transmission; the total radiated sound power is found by integrating the intensity over the surface S:

$$W = \int_{S} I(Q)\, dS(Q). \tag{3.3}$$

3.2.3 Sound Radiation Efficiency

The radiation efficiency, σ, is the ratio of the sound power radiated by a vibrating structure to the sound power that would be radiated by an equivalent flat piston vibrating in an infinite baffle:

$$\sigma = \frac{W}{\rho_0 c S \langle v^2 \rangle}, \tag{3.4}$$

where c is the speed of sound and $\langle v^2 \rangle$ is the mean square velocity of the surface S.

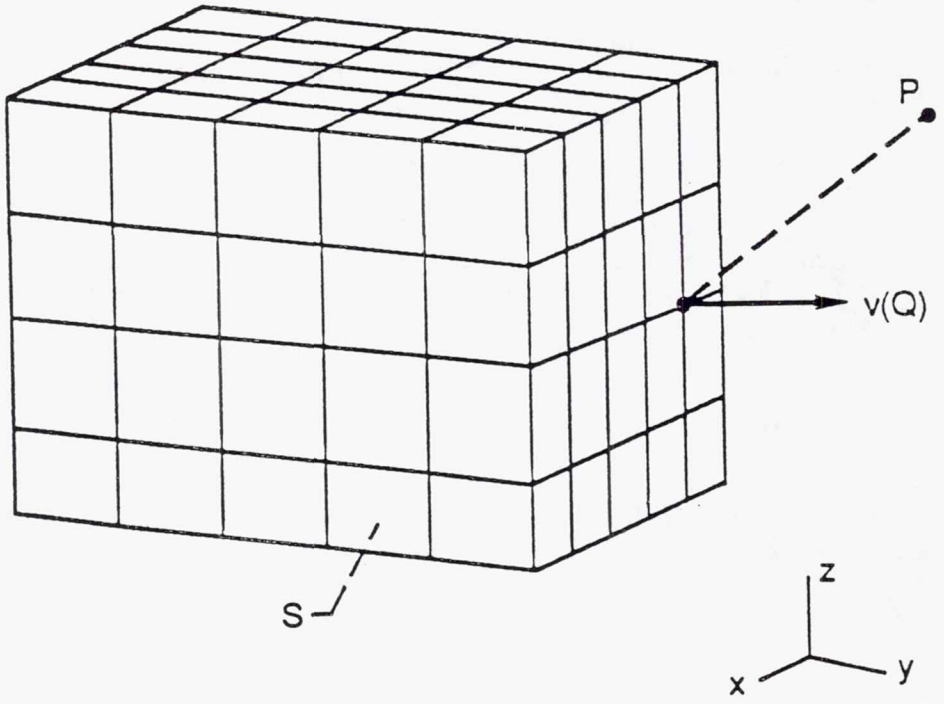

Figure 3.4 Gearbox with mesh showing BEM parameters.

3.2.4 The BEMAP Program

In this study, the BEMAP program [43] was used to perform the acoustical analysis described above. BEMAP is represented schematically in the flow chart shown in Fig. 3.5. The input to BEMAP is the surface geometry of the structure (the transmission), the vibration of the structure, and the frequency of vibration. The vibration data may originate from modal analysis experiments, as in the present study, but analytical vibration data, e.g., from finite element analyses, and the forced vibration data, may also be used. The vibration data may be normalized, as in the case of mode shapes, or absolute, as when the data is obtained from tests or from finite element, forced vibration models. Regardless of the source of the vibration, the magnitude and phase of the vibration at a discrete number of surface points (nodes) must be provided. The spacing of the nodes depends on the variation of the vibration data on the surface, the shape of the surface, and the frequency.

To simplify the transfer of vibration data and surface shape into BEMAP, a number of software interfaces have been written. An interface from an experimental modal analysis software package was used in the present study to import the grid point coordinates and modal data, e.g., Figs. 3.2 and 3.3, into BEMAP. Similar interfaces have been developed for importing vibration data from several popular finite element programs.

The output from BEMAP is the sound pressure and sound intensity on the surface of the structure, the sound power radiated by the structure, the radiation efficiency of the structure, and the sound pressure at any point in the acoustic field surrounding the structure. It should be noted that when the vibration of the surface $\{v\}$ is normalized (i.e., a mode shape), the sound pressure and sound intensity determined in Eq. (3.1) and Eq. (3.2) are relative values. In this case, the relative sound pressure and sound intensity distributions on the surface may be used to understand how a given mode radiates sound energy (i.e., which regions of the surface are responsible for radiation).

The radiation efficiency σ Eq. (3.4), is a function of the mode shape and the frequency of vibration. Even though a mode shape is a normalized vibration, σ is an absolute value; specifically, it is a property of the mode. Therefore, the radiation efficiency may be used to compare the sound-radiating characteristics of different structural modes.

3.3 Results

3.3.1 Transmission Housing Modes

To illustrate how the acoustical analysis described above may be applied to structural vibration, the two transmission housing modes in Figs. 3.2 and 3.3 are used as examples. In mode shown in Fig. 3.2, the 658 Hz mode, the top, front and rear surfaces of the transmission housing are vibrating in-phase (i.e., outward) with one another, while the two end surfaces are vibrating in-phase with each other (i.e., inward) but out-of-phase with the other three surfaces. (The bottom of the housing was much thicker than the other surfaces, and was rigidly attached to the frame supporting the transmission, therefore, it had negligible motion. Throughout this paper, the vibration of the bottom surface and the support frame are neglected.)

In the mode in Fig. 3.3, the 2722 Hz mode, most of the deflection is in the top surface of the transmission, with a small amount of deflection on the ends and virtually no motion on the front and rear surfaces. Considered as a plate, the top surface is vibrating in a 4,1 bending mode.

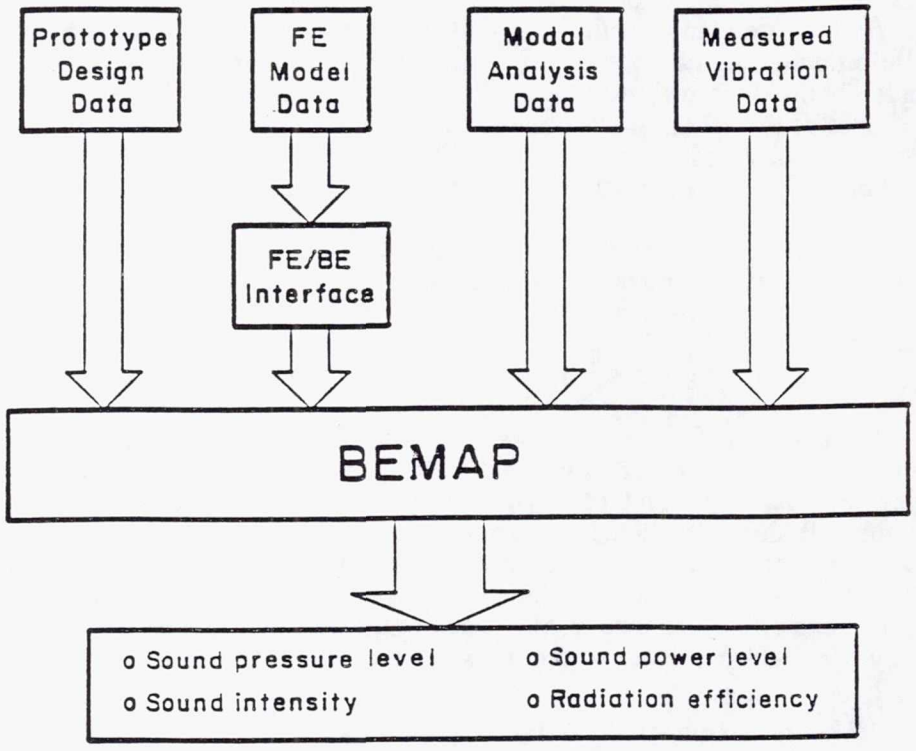

BEMAP Input Data Options and Output Quantities Determined

Figure 3.5 Inputs and outputs for the BEMAP program.

3.3.2 Sound Pressure and Sound Intensity Distributions

The relative sound pressure level distribution on the surface of the transmission for the 658 Hz mode (Fig. 3.2) is shown in Fig. 3.6. The relative sound pressure level varies from the highest value where the deflection is at maximum (near the center of each surface of the housing) to the lowest value at the vertical edges of the housing, a total variation of 30 dB. Each of the color bands in Fig. 3.6 represents a 3.5 dB change in sound pressure level.

The relative sound intensity distribution of the 658 Hz mode is shown in Fig. 3.7. By viewing the sound intensity distribution, one may see the "hot spots" where sound energy is radiated from the housing. Because the sound intensity is the sound power per unit area, it is a better indicator than the sound pressure level of the sound energy radiated by the mode. For example, the right end of the housing does not contribute as much to the total sound power as the top surface, as seen from Fig. 3.7. However, the opposite conclusion would be drawn from looking only at the sound pressure distribution in Fig. 3.6.

The relative sound intensity distribution for the 2722 Hz mode (in Fig. 3.3) is shown in Fig. 3.8. (Recall that this distribution cannot be compared quantitatively to the intensity distribution in Fig. 3.7 because each mode shape is normalized by the maximum deflection of that mode.) It is clear from Fig. 3.8 that there is a broad region on the top surface of the housing where sound energy is radiated. This is in spite of the appearance of the mode, Fig. 3.3, which would indicate that considerable cancellation should occur near the center of the top surface.

3.3.3 Radiation Efficiency

The radiation efficiencies of the eight transmission housing modes are shown in Fig. 3.9. As seen, all of the modes are very efficient radiators of sound. An approximate analysis using plate theory by Wallace [44] can be used to check the results in Fig. 3.9. This theory is strictly valid only for simply-supported plates in an infinite baffle, which is based on the ratio k/k_b of the acoustic and bending wave numbers. The acoustic wave number $k = \omega/c$ and the bending wave number is

$$k_b = [(m\pi/a)^2 + (n\pi/b)^2]^{1/2}, \qquad (3.5)$$

where a and b are the dimensions of the plate and m,n is the mode number. When $k/k_b << 1$, the radiation efficiency is much less than unity and highly dependent on mode number m,n. When $k/k_b \approx 1$, the radiation efficiency is less strongly affected by the mode number and approaches unity. Above $k/k_b = 1$, the radiation efficiency of each mode reaches a maximum value of between one and two and then decreases monotonically to unity for $k/k_b >> 1$.

In Fig. 3.10 the radiation efficiencies of seven of the eight transmission housing modes are compared to the radiation efficiencies of a rectangular plate [44] having the same dimensions as the top surface of the transmission housing. (The 2000 Hz mode was omitted as it did not exhibit a dominant plate mode on the top surface of the transmission housing.) The plate mode number is shown for each of the data points in Fig. 3.10. It

Page intentionally left blank

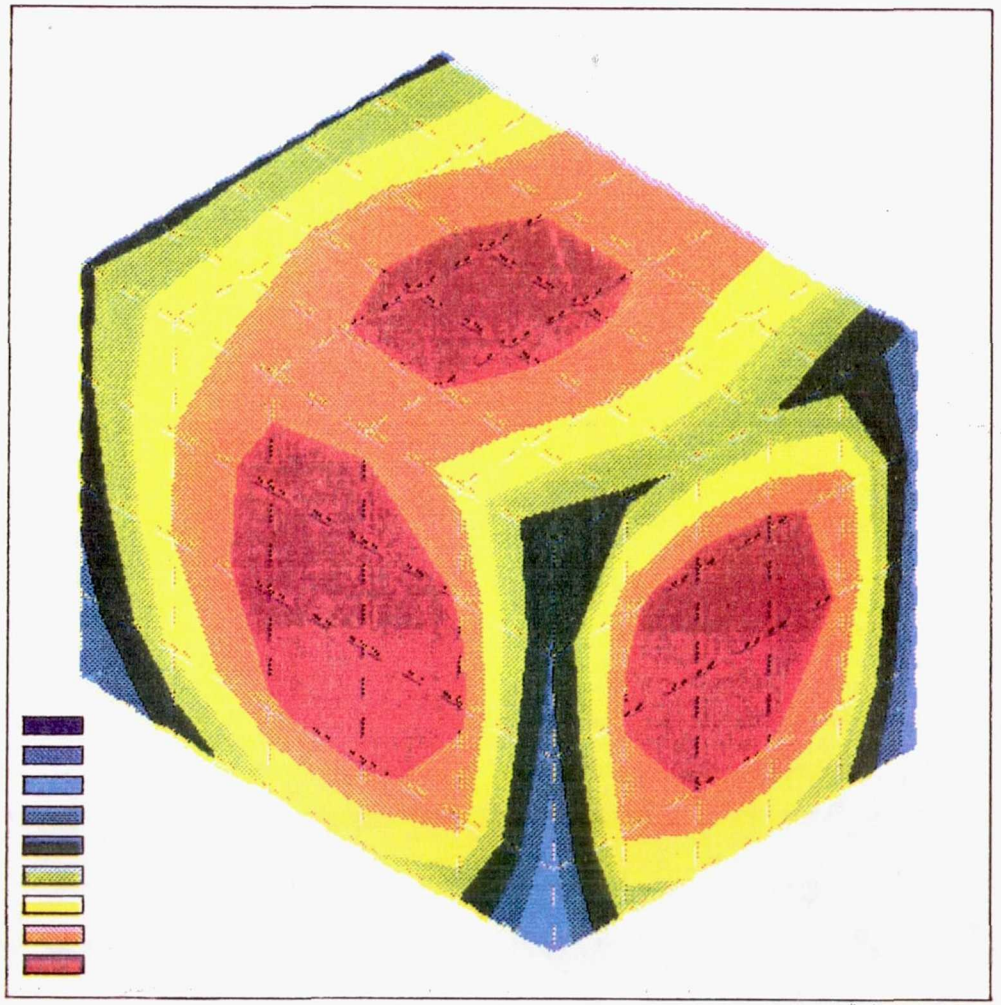

Figure 3.6 Relative sound pressure level distribution on the surface of the transmission housing for the 658 Hz mode. Red color represents the maximum value, each color band represents a 3.5 dB change.

Page intentionally left blank

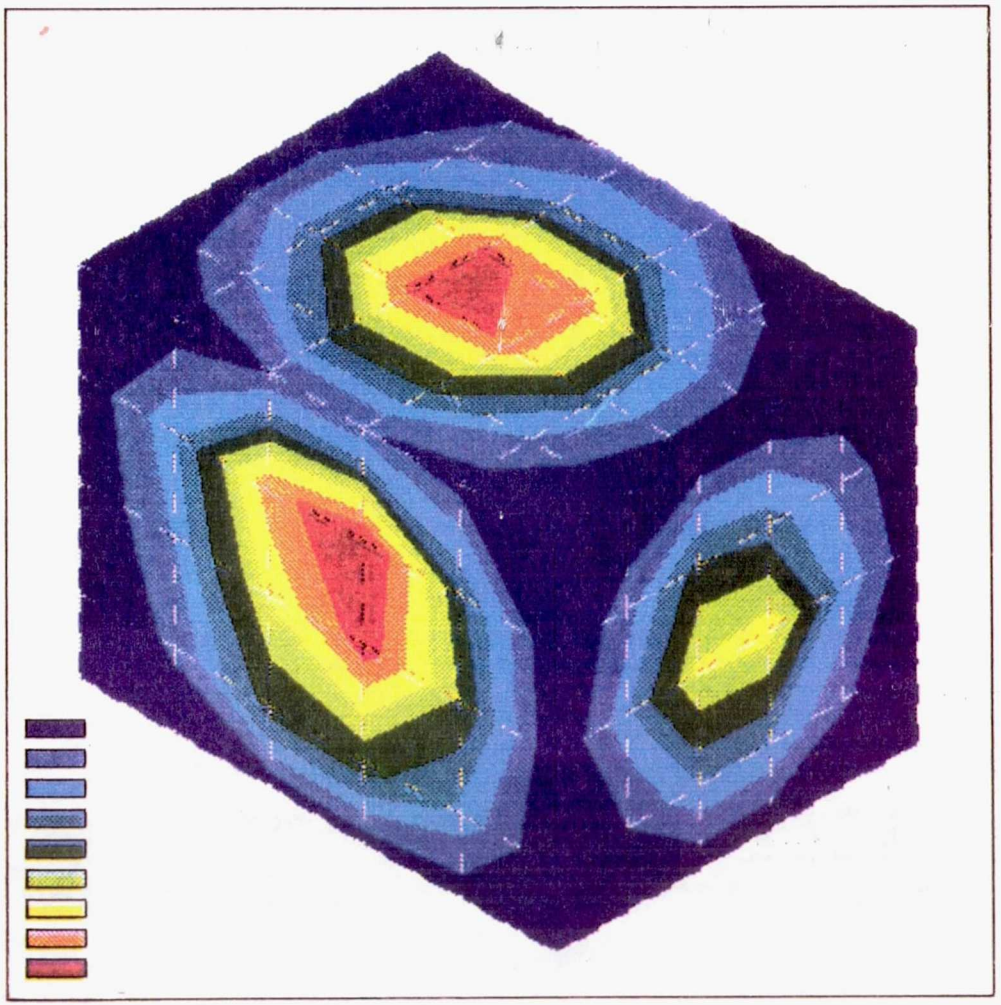

Figure 3.7 Relative sound intensity distribution on the surface of the transmission housing for the 658 Hz mode. Red color represents the maximum value, each color band represents a 1.4 W/m^2 change.

Page intentionally left blank

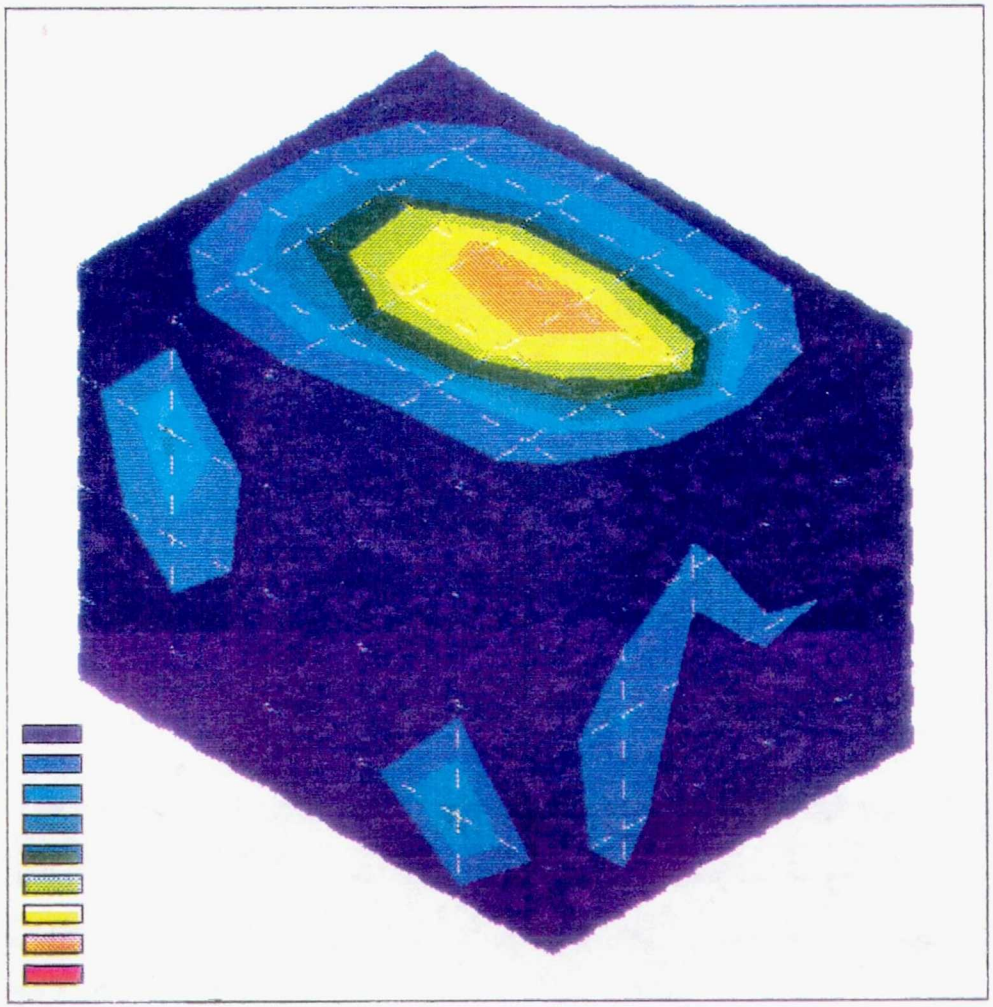

Figure 3.8 Relative sound intensity distribution on the surface of the transmission housing for the 2722 Hz mode. Red color represents the maximum value, each color band represents a 3.2 W/m^2 change.

Page intentionally left blank

Figure 3.9 Radiation efficiency of the eight transmission housing modes.

may be seen from Fig. 3.10 that the wave number ratio for all of the modes lies between 0.75 and 1.35, the region where the radiation efficiency is the highest.

The two sets of data in Fig. 3.10 follow the same trend. The data in Fig. 3.10 illustrate that the transmission housing is dominated by modes which resemble those of a flat panel. However, because the top surface of the housing is not baffled, and because there is radiation from the other surfaces of the transmission, there are some discrepancies between the theoretical data for a baffled plate and the gearbox data.

3.4 Structural Modfication and Noise Control

Structural modification of the transmission housing is a logical method of noise control. In general, modifications which stiffen a vibrating structure would tend to reduce vibration because the natural frequencies are pushed to higher frequencies where, presumably, the spectrum level of the forces exciting the structure is less. However, this simplistic approach ignores the effect of radiation efficiency on the radiation of sound from the vibrating structure. It is clear from Eq. (3.4) that the sound power is directly proportional to the radiation efficiency. Thus, while modification of the structure may reduce the mean-square vibration $\langle v \rangle^2$ the radiation efficiency may increase.

Consider the effect of a straightforward modification in which the thickness of the transmission housing is altered. This would have the effect of changing the natural frequencies of the modes without materially altering the mode shapes. (A similar effect may be obtained by changing the composition of the transmission housing material.) To see the effect of such a modification, the radiation efficiency of each mode is determined at frequencies above and below the measured value. These data are plotted in Figs. 3.11 and 3.12 for the 658 Hz and 2722 Hz modes, respectively, in which the measured natural frequency of each mode is represented by the filled data symbol.

The radiation efficiency of the 658 Hz mode increases with frequency, as shown in Fig. 3.11. Thus, a thicker transmission housing will radiate more noise if the reduction of vibration level does not offset the increase in radiation efficiency. It is also possible that thickening of the transmission housing may move a mode with a high radiation efficiency from a frequency where it is not excited to a new frequency (e.g., a gear mesh frequency) where it may radiate considerably more sound energy.

By contrast, the radiation efficiency of the 2722 Hz mode is almost independent of frequency, as seen in Fig. 3.12. Thickening of the housing will not increase the radiation efficieny of this mode and, unless the new frequency coincides with a gear mesh frequency, the sound energy radiated by this mode will decrease.

3.5 Summary and Discussion

Transmission housing vibrational modes may be analyzed acoustically to determine their impact on the sound energy radiated by the transmission. The BEM may be used to determine the sound intensity on the surface of the transmission housing and the radiation efficiency of each mode in order to assess the importance of each mode acoustically. The BEM may also be used to examine "what if" strategies for structural modification such as altering the thickness or changing the material composition of the transmission housing.

In this chapter, the BEM has been used to analyze the radiation characteristics of the structural modes of the gear test rig developed by NASA. The radiation efficiency of each

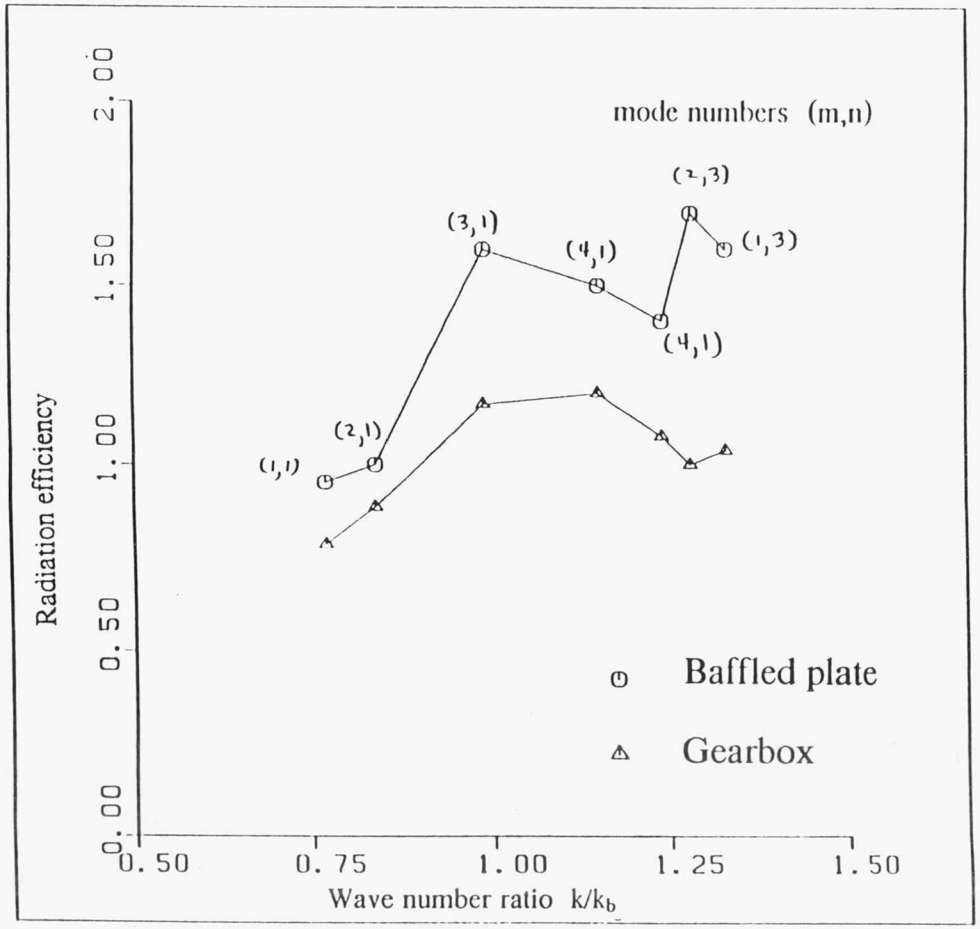

Figure 3.10 Radiation efficiency calculated using BEMAP and using plate theory.

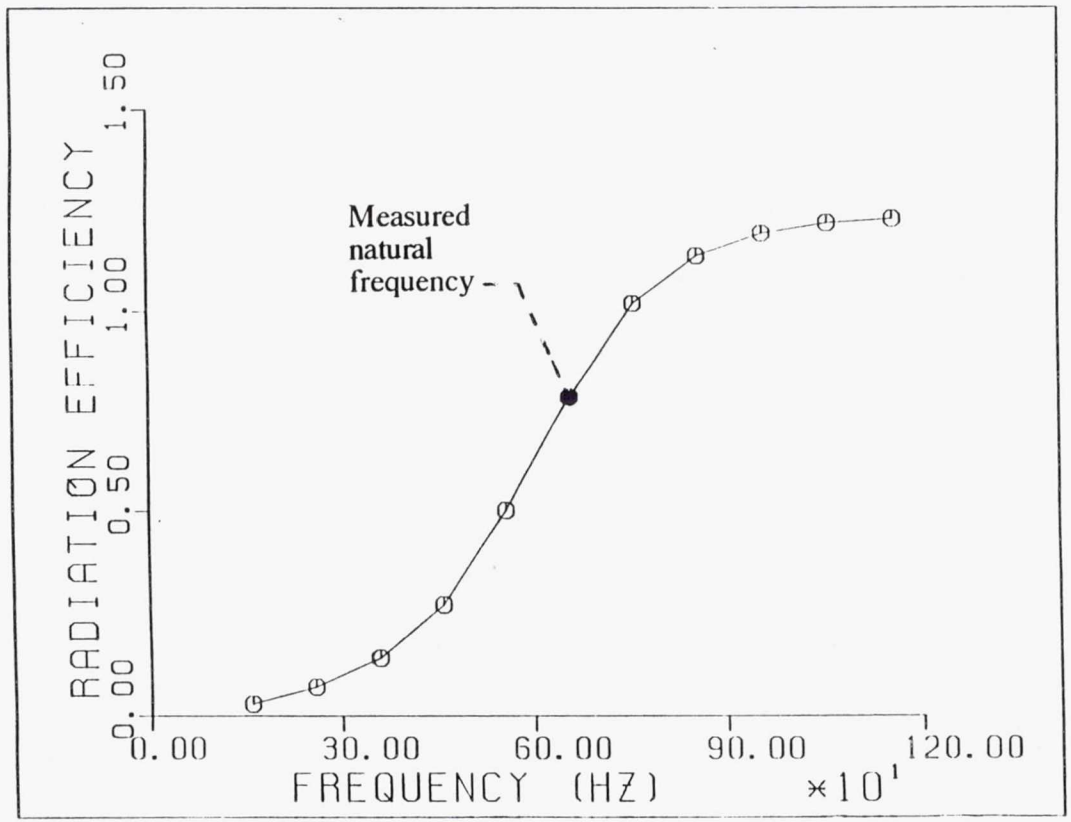

Figure 3.11 Radiation efficiency of the 658 Hz vibration mode as a function of natural frequency.

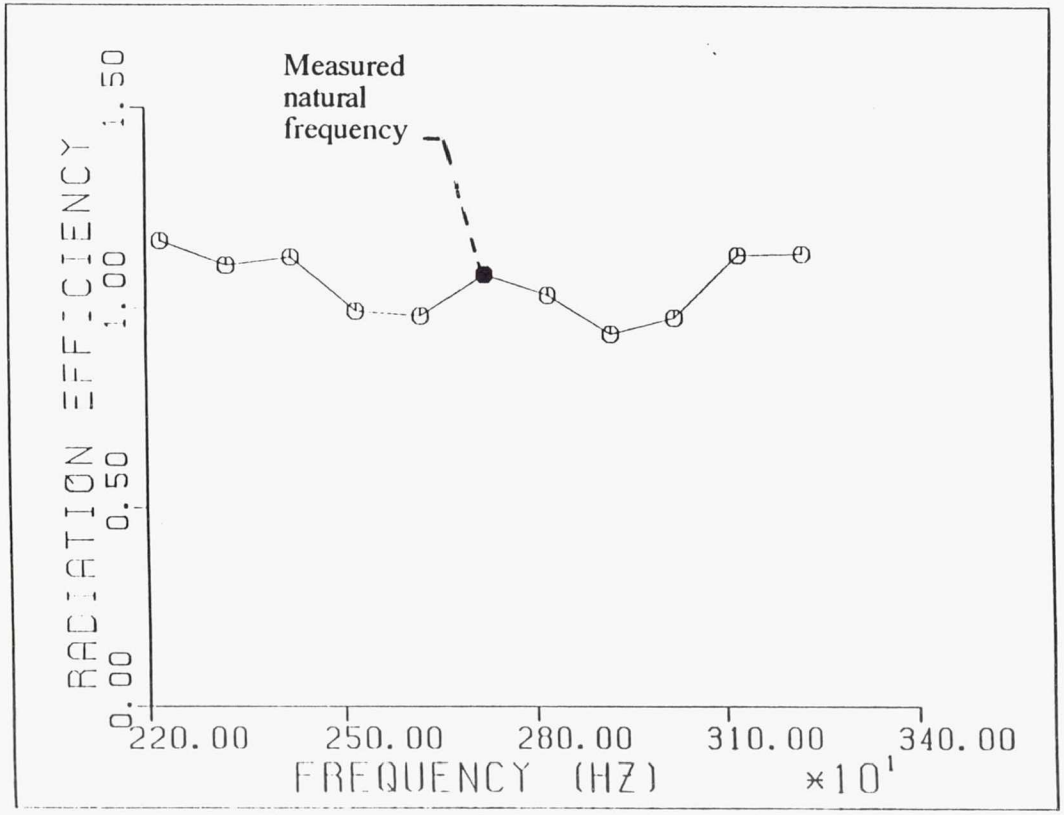

Figure 3.12 Radiation efficiency of the 2722 Hz vibration mode as a function of natural frequency.

mode was determined and compared to the approximate values in [44], based on the plate radiation theory.

Because the transmission housing modes are similar in appearance to those of simple rectangular plates, the plate radiation theory was partially successful in estimating the radiation efficiency of the transmission housing modes. The present approach of calculating the radiation efficiency of each mode using the BEM is superior because, unlike the plate radiation theory, the BEM makes no assumptions about boundary conditions, baffling or uniformity of the mode shapes.

CHAPTER 4

VALIDATION OF FEM/BEM PREDICTED STRUCTURAL VIBRATION AND RADIATED NOISE

4.1. Introduction

In this chapter, an experimental validation of FEM/BEM predicted structural vibration and radiated noise is presented. First, a FEM model of the vibrating structure was constructed using the commercial FEM software package ANSYS. Using this model, the vibration of the structure at each nodal point was predicted. Experimental model analysis data was used to check the validity of this model. The validation included comparison of the natural frequencies, comparison of the mode shapes, and comparison of the transfer functions at certain points of the structure. The natural frequencies derived from theoretical calculation were also compared with the experimental and FEM results. Once the FEM model was validated, it was used to determine the velocity and displacement of the structure at each nodal point in the frequency range of 100-500 Hz.

Additionally, the nodal velocities or displacements of the structure can be determined by experimentation. In this research, an accelerometer was used to measure the acceleration of the structure at each nodal point. The velocity or displacement was then determined by integration once or twice.

At this point, two sets of vibration data are available to evaluate the radiated noise: vibration data from the FEM model and vibration data from the experiments. These two sets of vibration data were used as input to predict the radiated noise using BEM. Two interface codes were written and used to transform the FEM predicted vibration data and the measured vibration data to the format needed for input into the BEM code BEMAP. BEMAP then calculated the total radiated sound power and radiation efficiency of the vibrating structure. Again, two sets of data were obtained; one was the total radiated sound power and radiation efficiency from the FEM-predicted vibration, the other was those predicted from measured vibration.

Once the radiated noise was predicted, the final step was to validate it by experimentation. As discussed earlier, the total radiated sound power is used as the validation quantity. In the present study, the total radiated sound power was measured by the sound intensity method using a commercial sound intensity measurement system. To validate only the BEM portion of the prediction, the total radiated sound power predicted from measured vibration was compared with the measured total radiated sound power. To validate the entire FEM/BEM prediction process, the total radiated sound power predicted from FEM vibration was compared with the measured total radiated sound power.

4.2 Sound Intensity Method

4.2.1 General

In ordinary sound measurements, a microphone is used to measure sound pressure. The sound pressure produced by a noise source depends not only on the sound energy radiated by the source, but on the environment in which the source is placed and the position of the microphone relative to the source. Thus, while being a useful quantity, sound pressure is not an adequate means to characterize a noise source. Since the sound power of the source is the rate at which the source radiates sound energy, the sound power is a characteristic of the source, and therefore, is a more meaningful quantity to use in

characterizing a noise source. However, sound power cannot be measured, instead, it must be determined indirectly from other measurements.

Sound power is a product of the average sound intensity over any surface enclosing the source, times the area of that surface. How to effectively determine sound power has been a fundamental problem in acoustics for decades. Until the sound intensity method was developed, sound power could only be determined in special acoustical environments, such as reverberation or anechoic chambers. In such environments there is a simple relationship that exists between sound pressure and sound intensity, and thus the sound power can be determined by measuring sound pressure.

In ordinary sound measurements, a single microphone is used to measure the sound pressure. In the sound intensity method, a pair of closely-spaced microphones is used to measure the sound intensity at a point midway between the microphones. From a number of such measurements, the average sound intensity over a surface can be determined. If this surface totally encloses the noise source, the sound power is determined by multiplying the average sound intensity by the area of the surface.

The idea of using two closely-spaced microphones to estimate the sound intensity at a point is not new. It has been suggested many times in the past half century. However, it was not until the last decade that the practical implementation of the sound intensity method became feasible with the introduction of the two-channel FFT analyzers. The main advantage of the sound intensity method (SIM) over other methods of determining sound power is that no special acoustical environment is required. This means that field measurements of sound power are now possible, and in most cases, an ordinary laboratory room or test chamber may be used. A second advantage of SIM is that measurements may be taken even when background noise is relatively high. A major rule to follow for the conventional sound pressure measurement to be valid is that the background noise level should be approximately 10 dB less than the level of the source. A valid sound intensity measurement can be made even when the background noise exceeds the noise level of the source.

4.2.2 Modern Formulation for Intensity Measurement

For a stationary ergodic signal, the acoustic intensity, I_r, at a location in the sound field in a given direction, r, can be expressed as [45, 46]

$$I_r = E\{p \cdot u_r\}, \tag{4.1}$$

where E denotes the expected value and p and u_r are the acoustic pressure and the component of the acoustic velocity in the r direction, respectively. For the complex pressure, $\mathbf{p}$, and the complex velocity $\mathbf{u}_r$, the sound intensity can be expressed as

$$I_r = \frac{1}{4} E\{(\mathbf{p} + \mathbf{p}^*)(\mathbf{u}_r + \mathbf{u}_r^*)\}, \tag{4.2}$$

where * denotes the complex conjugate. Equation (4.2) can be rearranged into

$$I_r = \frac{1}{2} E\{Re(\mathbf{p} \cdot \mathbf{u}_r) + Re(\mathbf{p} \cdot \mathbf{u}_r^*)\}, \tag{4.3}$$

where Re denotes the real part.

In the frequency domain, when both $\mathbf{p}$ and $\mathbf{u}_r$ are represented by their Fourier components, equation (4.3) becomes

$$I_r(\omega) = \frac{1}{2} E\{Re(p(\omega) \cdot u_r(\omega)) + Re(p(\omega) \cdot u_r(\omega)^*)\}, \tag{4.4}$$

where ω is the angular frequency and, e.g., $p(\omega)$ denotes the Fourier transform of $\mathbf{p}$.

Consider two closely spaced microphones with a separation distance, Δr, in the r direction. Let p_1 and p_2 be acoustic pressure measured at the first and second microphone, respectively. From Eq. (2.1), the linear Euler's equation with no flow and no viscous dissipation, one has the basic pressure-velocity relation

$$\mathbf{u}_r = -\frac{1}{\rho_0} \int \frac{\partial \mathbf{p}}{\partial \mathbf{r}} \, dt, \tag{4.5}$$

then the Fourier transform of $\mathbf{u}_r$ at a point midway between the microphones may be approximated as

$$u_r(\omega) = i\,(p_2(\omega) - p_1(\omega)) / \rho_0 \Delta r \omega, \tag{4.6}$$

where ρ_0 is the density of air and $i = (-1)^{1/2}$. The Fourier transform of the pressure at the midpoint location may be expressed as

$$p(\omega) = \frac{1}{2}(p_1(\omega) + P_2(\omega)). \tag{4.7}$$

Substituting Eqs. (4.6) and (4.7) into Eq. (4.4) gives

$$I_r(\omega) = [\, E\{Re(p_1(\omega)) \cdot Im(p_1(\omega)) - Re(p_2(\omega)) \cdot Im(p_2(\omega))\} + E\{Im(p_1(\omega) \cdot p_2(\omega)^*)\}]/2\rho_0 \Delta r \omega, \tag{4.8}$$

where Im indicates the imaginary part. For stationary and ergodic signals,

$$E\{Re(p_1(\omega)) \cdot Im(p_1(\omega))\} = 0, \tag{4.9}$$

and

$$E\{Re(p_2(\omega)) \cdot Im(p_2(\omega))\} = 0 \tag{4.10}$$

and it follows immediately that the acoustic intensity spectrum is

$$\begin{aligned} I_r(\omega) &= E\{Im(p_1(\omega) \cdot p_2(\omega)^*)\}/2\rho_0\Delta r\omega \\ &= Im\{G_{12}\}/2\rho_0\Delta r\omega, \end{aligned} \tag{4.11}$$

where G_{12} is the cross spectrum between p_1 and p_2.

4.2.3 Phase Calibration

In the sound intensity method, the sound intensity, I_r, at a point in direction, r, is estimated by Eq. (4.11)

$$\begin{aligned} I_r(\omega) &= Im\{G_{12}\}/2\rho\Delta r\omega \\ &= |G_{12}| \frac{\sin\phi_{12}}{2\rho_0\Delta r\omega}, \end{aligned} \tag{4.12}$$

where ϕ_{12} is the phase angle between the microphone signals. From this expression one can notice that the error in the measurement of ϕ_{12} is a significant error source of the sound intensity method. So the phase mismatch between measurement channels must be very low (typically less than 0.5 degree) to ensure valid sound intensity measurements. Phase mismatch has two main sources: phase mismatch within the analyzer and phase mismatch between the microphones used in the measurements. In the present study, the phase mismatch within the intensity measurement package was less than 0.2 degree because every board set had been phase calibrated by the manufacturer. There are two ways to avoid the possibility of errors caused by microphone phase mismatch. One is to use a special set of "phase matched" microphones, or a phase calibration can be performed on microphones that are not phase matched. In the present study, the microphone phase mismatch was corrected by performing phase calibration. A specially designed phase calibration tube was used to calibrate the microphones. The microphones were mounted in one end of the tube, and a high-quality acoustic driver was mounted at the other end. Broadband random sound from the driver was used to determine the phase mismatch between the microphones.

4.2.4 The Sound Intensity Floor and Dynamic Range

The "sound intensity floor", the smallest value of sound intensity that can be measured in a given measurement situation, depends on the sound environment and the phase mismatch of the measurement channels. The sound intensity floor, L_{floor}, in decibels is given by [47]

$$L_{floor}\,(dB) = L_p - 10 \log (\omega \Delta r / c \Delta \phi), \qquad (4.13)$$

where L_p is the sound pressure level (dB re 20 μPa), c is the speed of sound, and $\Delta\phi$ is the phase mismatch between the measurement channels.

The difference between the sound intensity level and the intensity floor is an indicator of the validity of the sound intensity measurement. Usually this difference should be larger than 5 dB. In the present study, in the frequency range 100-500 Hz, the difference is larger than 5 dB at lower frequencies to larger than 15 dB at higher frequencies. Reducing the reverberant sound field or the background noise will usually increase the difference between the intensity level and the intensity floor.

For a plane wave sound field, or in the farfield of a source, the sound intensity level and the sound pressure level will have the same numerical value. Therefore, the "dynamic range" of sound intensity is the difference between the sound pressure level and the intensity floor, i.e., the last term in Eq. (4.13). Using a phase error of about 0.1 degree and a microphone spacing of about 50 mm, the dynamic range is about 24 dB at 500 Hz and 18 dB at 100 Hz.

4.3 Measurements

4.3.1 General

The experiment discussed herein was designed to validate the vibration and noise prediction based on the FEM and the BEM. The experimental apparatus is shown schematically in Fig. 4.1. The structure is a rectangular box of overall dimension 11 inches × 12 inches × 11.75 inches with only the top plate being flexible; the other five surfaces are much more massive and stiffer than the top plate and are assumed to be rigid. The top plate is made of 1/16-inch aluminum, and the other five surfaces are made of 1/2-inch thick steel. Four strips of 1/2-inch square steel rod are used to attach the top plate to the edges of the four side plates in order to approximate clamped boundary conditions.

4.3.2 Vibration Measurements

A shaker was mounted inside the structure to excite the top plate. A random excitation signal was used to drive the shaker. An impedance head was used to measure the applied force and the driving point acceleration. An accelerometer was used to collect the acceleration at various points on the top plate. The weight of the accelerometer was about 1.3 grams. To ensure that the force was applied in a direction perpendicular to the top plate, a stinger (Fig. 4.2) made of piano wire was connected the impedance head to the top plate. This connection was found to be very effective in minimizing the excitation in directions other than perpendicular to the top plate. The experimental apparatus was set on the floor to create a half-space radiation condition.

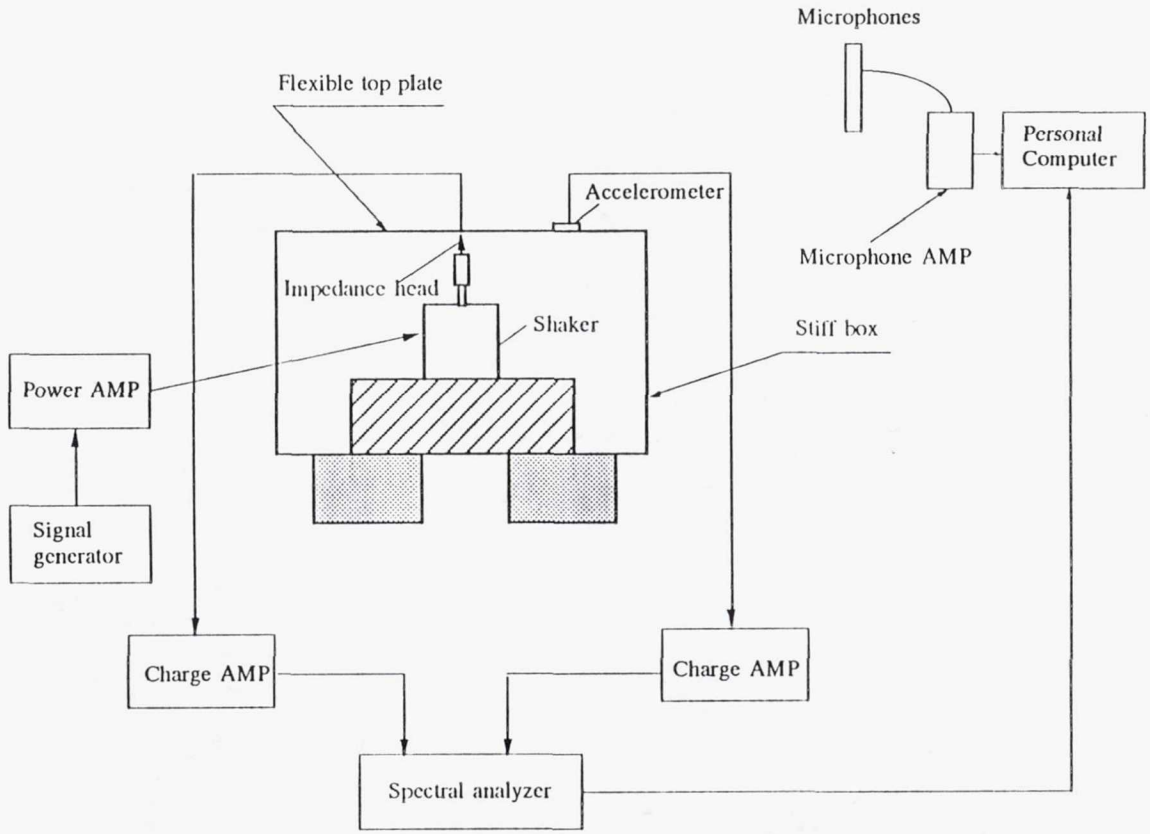

Figure 4.1 Experimental setup .

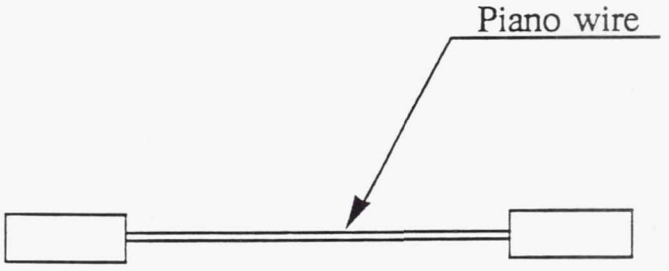

Figure 4.2 Stinger used in the experiments.

A two-channel dynamic signal analyzer was used to collect calibrated acceleration data normalized by the input force of the shaker. Two charge amplifiers were used to amplify and condition the signals before they entered the analyzer. The data in the analyzer was then transferred to a personal computer and written to disk. A FORTRAN data acquisition code was used to perform the above process. The acceleration data was used in two ways: to validate the acceleration data predicted by FEM and as the boundary condition to the BEM program BEMAP. An interface program was written to transfer the vibration data into a standard BEMAP input file.

4.3.3 Sound Intensity Measurements

There are two ways to determine the sound power by sound intensity measurements. One is the sound intensity measurement at discrete points, the other is the sound intensity measurement by scanning. Since it is quicker and more convenient than fixed point measurements, scanning measurements were used in the present study. A 20 inches × 20 inches × 20 inches wire frame was used to define the sweeping surface (Fig. 4.3). In the scanning process, the signal analyzer was set to time-average the measured quantity over the period of each traverse, thus forming of a set of parallel line sweeps, which were then repeated with an orthogonal orientation, so that each section of the source was covered at least twice.

A commercial intensity measurement package was used to measure the sound intensity and to calculate the total radiated sound power. The spacing between the two microphones in the probe was two inches. This spacing was chosen to assure that the frequency range in the present study was within the measurement frequency range of the probe. The measured sound intensity and total radiated sound power were normalized by the square of the input force, which was taken from the impedance head and acquired by a personal computer through the signal analyzer. This made it possible to directly compare the measured sound power with that predicted by the FEM/BEM model.

Phase calibration was performed to correct the phase mismatch between the two microphones. A specially designed tube (Fig. 4.4) was used to perform the phase calibration. The microphones were mounted at one end of the tube, and a high quality acoustic drive was mounted at the other end. This acoustic drive was used to produce broadband random noise, which when traveling inside the tube, is a plane acoustic wave. If both microphones are mounted flush with the end flange of the tube (Fig. 4.5), the phase between the two measured signals is the phase mismatch of the microphones. This phase mismatch can then be used to correct the measured phase angle during the sound intensity measurements.

4.4 FEM/BEM Models

4.4.1 Finite Element Model

The flexible top plate of the apparatus in Figure 4.1 was modeled using the FEM program. Clamped boundary conditions were used along the edge of the plate. One hundred quadrilateral quadratic thin-shell elements were used to model the top plate, and a unit force was applied to excite the plate. To model the mass below the force-sensitive crystal of the impedance head, the mass of the stinger, and the mass of two nuts, as shown in Fig. 4.6, another mass element was used. Two numbers were given as the values of the mass element. The first value was the mass described above, about 10 grams. This value was used to calculate the velocity or the acceleration, at each nodal points of the plate excited by the applied unit force. The second value was the sum of the mass of the

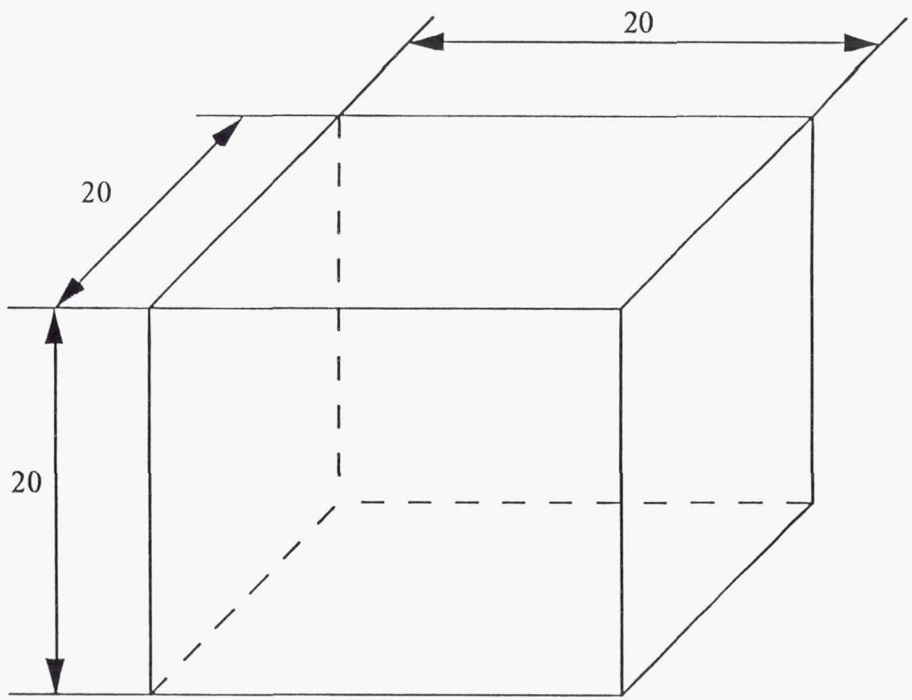

Figure 4.3 Frame used for sound intensity measurements .

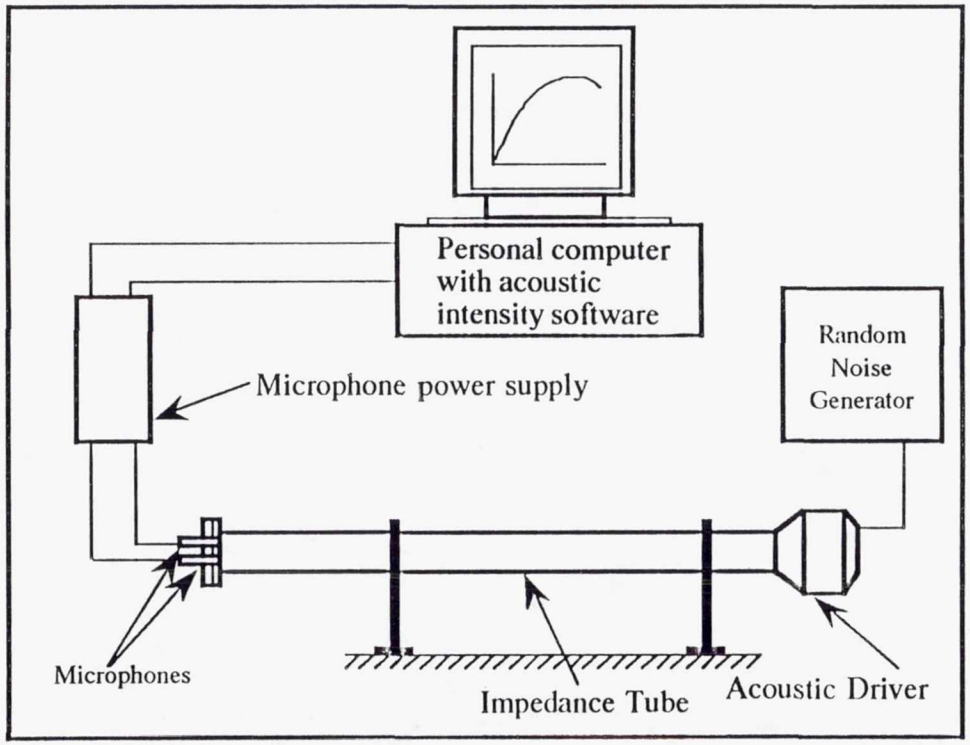

Figure 4.4 Impedance tube for microphone phase calibration .

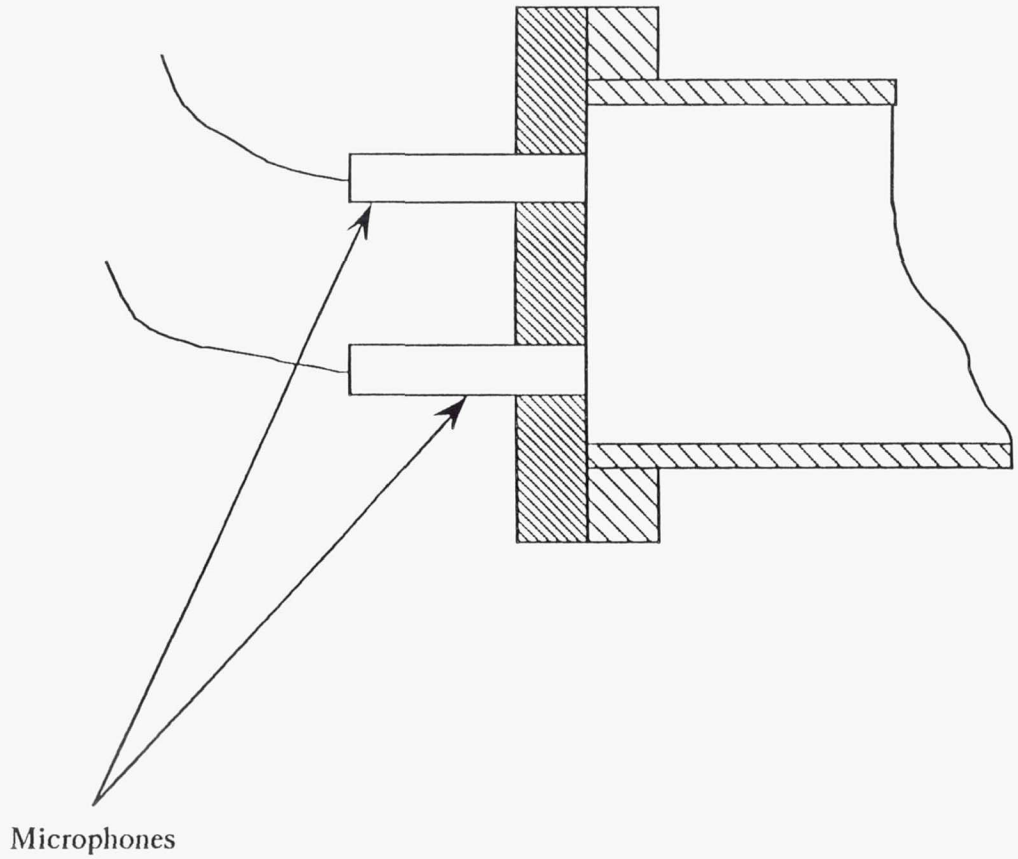

Figure 4.5 Position of the microphones in the impedance tube.

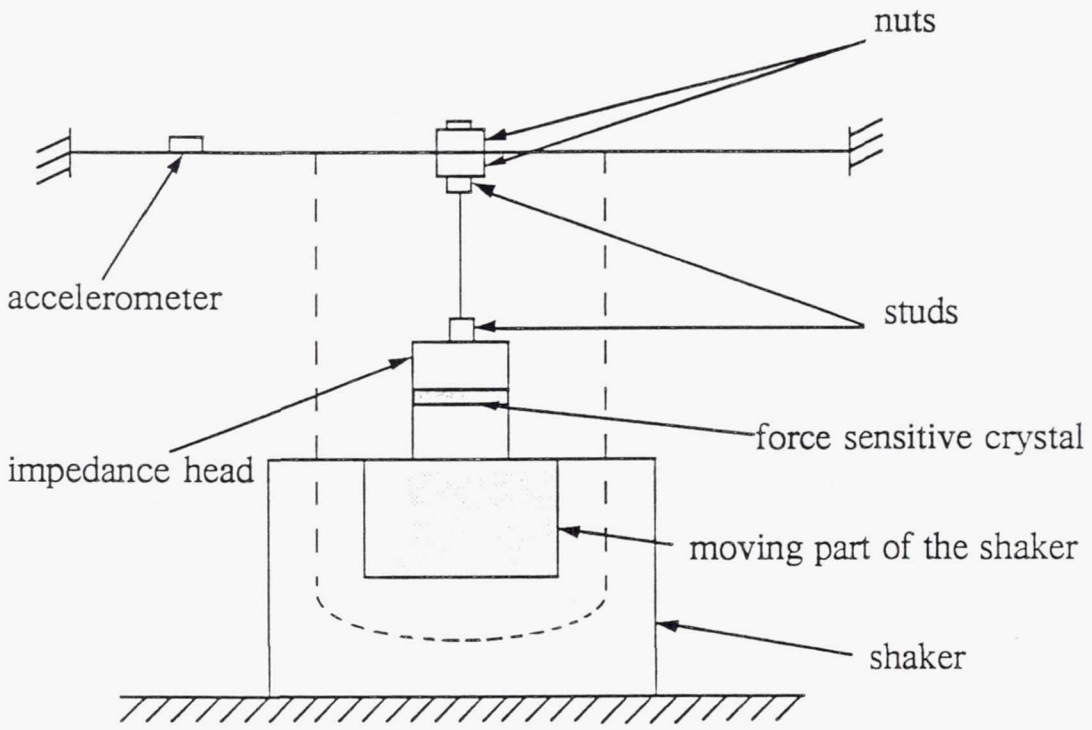

Figure 4.6 Mass to be included in the FEM model for the calculation of mode shapes.

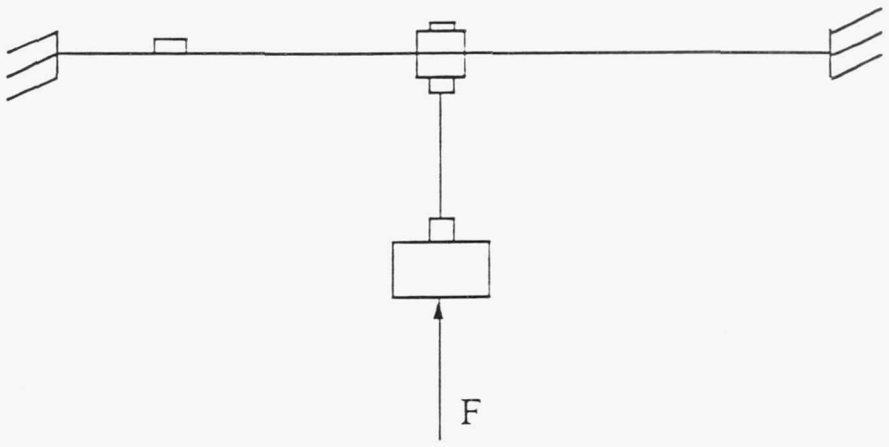

Figure 4.7 Mass to be included in the FEM model
for the calculation of transfer functions .

following: moving part of the shaker, 18 grams; impedance head, 29 grams; and the mass of the stinger and two nuts. The total value was about 54 grams. This value was used to calculate the mode shapes of the FEM model. The reasons for using two values are explained below.

The real system included the mass within the dashed line illustrated in Fig. 4.6, which amounted to about 54 grams. The mode shapes observed are the mode shapes of this system. To calculate the mode shapes, the mass within the dashed line must be included in the FEM mode, i.e., 54 grams must be used in the FEM model. However, when the transfer functions were taken, i.e., the accelerations were normalized by the applied force, the mass of the shaker was no longer a part of the system, as shown in Fig. 4.7.

On the other hand, the mass of the accelerometer (1.3 grams) was excluded from the FEM model. It was found that it had an insignificant effect on the structural dynamics in the frequency range of concern in this study.

The modal superposition method was used to compute the harmonic response of the FEM model. Four modes were found in the frequency range 100—500 Hz. Table 4.1(a) shows the natural frequencies obtained from both the FEM model and the experiments. The error in the table is defined as

$$\text{Error} = \frac{F_f - F_e}{F_f},$$

where F_f represents the frequency from the FEM model and F_e represents the frequency from the experiments.

It can be noted from Table 4.1(a) that the predicted and measured natural frequencies of the system agree well in the frequency range 100-500 Hz. However, a small shift existed between the two sets of data; the largest shift happened at the fourth resonance with a relative difference of 4.4 percent.

Table 4.1(b) shows the natural frequencies obtained theoretically [48] and those obtained from the FEM model (i.e., same as in Table 4.1(a)). The theoretical natural frequencies are for a clamped square plate with the same material and thickness as those used in the FEM model. In the FEM model, the dimension of the plate was 11 inches × 12 inches. In the theoretical calculation, a dimension of 11.5 inches × 11.5 inches was used. Another difference is that the FEM model has a concentrated mass, while the theoretical model does not. These two differences, in dimension and nodal mass, are the major sources contributing to the differences of the natural frequencies.

There was one resonance disappeared from the theoretical calculation. Apparently, this was due to the symmetry of the square plate. For a square plate, the second and the third mode (1-2 and 2-1) share the same natural frequency and mode shape.

Figure 4.8 illustrates the frequency response function (acceleration normalized by the applied force) at the driving point of the top plate of the box. The difference between the experimental data and the FEM data is mainly due to a shifting of the natural

Table 4.1

	Mode 1	Mode 2	Mode 3	Mode 4
Experimental	159(Hz)	293(Hz)	331(Hz)	457(Hz)
FEM	159(Hz)	301(Hz)	344(Hz)	478(Hz)
Error	0	2.7%	3.8%	4.4%

(a) Natural frequencies from measurements and FEM.

	Mode 1	Mode 2	Mode 3	Mode 4
Theoretical	160(Hz)		332(Hz)	489(Hz)
FEM	159(Hz)	301(Hz)	344(Hz)	478(Hz)
Error	0.6%		3.5%	2.2%

(b) Natural frequencies from theoretical calculation and FEM.

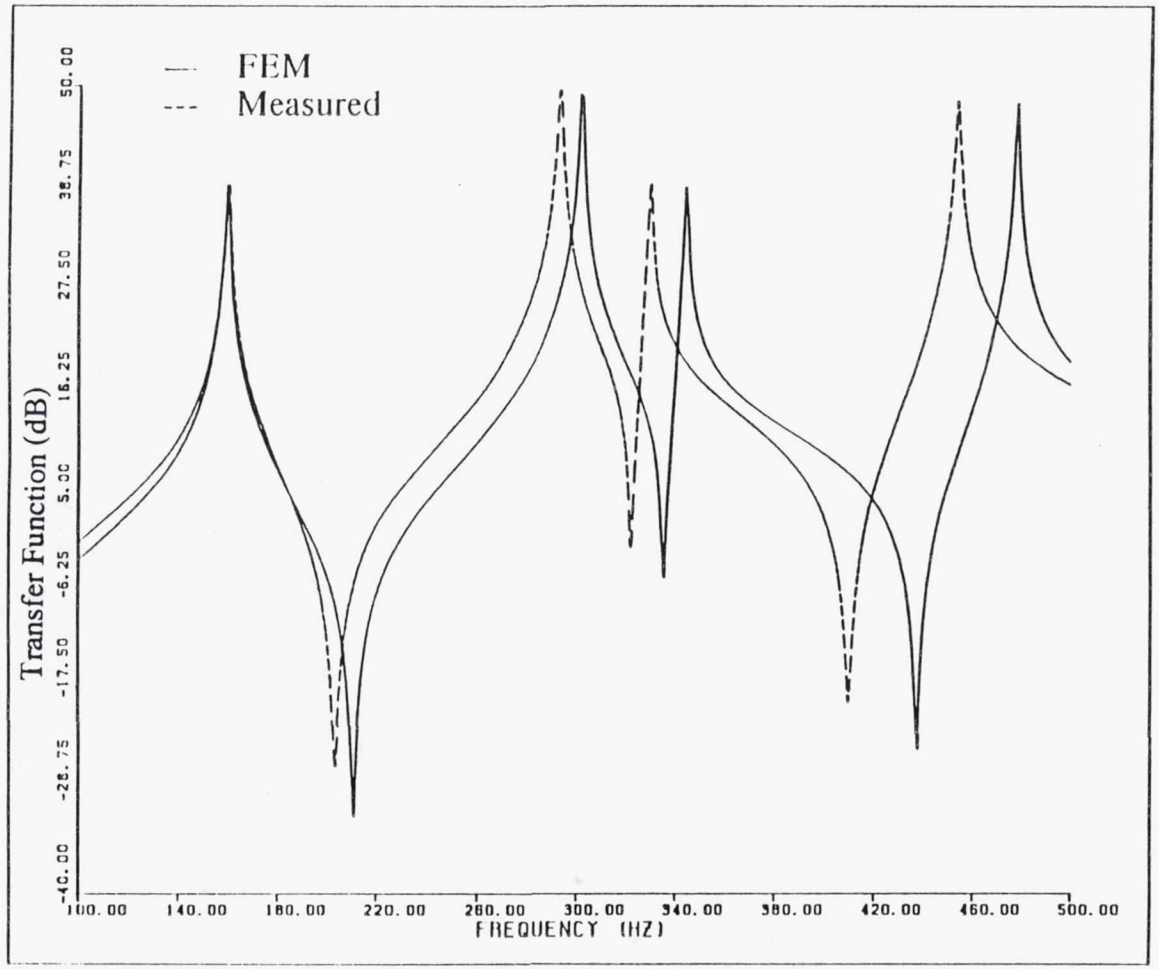

Figure 4.8 Frequency response function from modal superposition method.

frequencies. The largest shift of about 4.4 percent occurred at the fourth resonance, as discussed earlier.

There are several factors which affect the magnitude of experimentally-obtained frequency response functions. The response of a mechanical system is a superposition of responses of the individual structural modes. The magnitude of response of a structural mode depends on its modal dynamic properties, the magnitude of its mode shapes at the drive point and the magnitude of its mode shapes at the receiving point. These factors combine in a multiplicative way to determine the modal response. Since a mechanical frequency response function is a superposition of modal responses, the accuracy of the modal dynamics and mode shapes predicted by the finite element method determines the accuracy of the structural response.

The major reason for the shift of natural frequencies is that clamped boundary conditions are used in the FEM model for the top surface. The boundary conditions of the real system are not perfectly clamped, but lie somewhere between simple supported and clamped boundary conditions. Thus, the FEM model is stiffer than the real system.

There are four modes in the frequency range 100—500 Hz. All of the mode shapes obtained from the FEM model share the same trend and shape with their counterparts from the experiment. For example, Fig. 4.9(a) is the mode shape of the first mode calculated from the FEM model; Fig. 4.9(b) is a photograph of a sand pattern which shows the mode shape of the first mode from experiments; likewise, Figs. 4.9(c) and (d) show mode shapes of the second mode from the FEM and the experiment, respectively.

4.4.2 Boundary Element Model

Two BEM models were used to model the vibrating structure. One was for the measured vibration, and the other for the FEM-calculated vibration. The mesh used for the measured vibration was somewhat more coarse (i.e., less conservative) than the one used for FEM vibration in order to reduce the amount of time needed to acquire the data. For the measured vibration, the top plate of the structure was modeled by 36 quadrilateral quadratic elements, resulting in 85 nodes at which the normal surface velocity was measured. These vibration data were measured using the accelerometer shown in Fig. 4.1. The velocities at the grid points along the edge of the top plate were set to zero since the clamped boundary conditions were used in the FEM model. The other five surfaces were each modeled by 36 quadrilateral quadratic elements, as shown in Fig. 4.10(a). The total number of nodes for this BEM model was 650. All grid point velocities on the four side plates were assumed to be zero. This was only approximately true for the structure in the present study; a quick check showed that the magnitude of the vibration of the side plates was less than one tenth of that of the top plate.

For the FEM calculated vibration, the BEM mesh consisted of 100 quadrilateral quadratic elements on the top plate, resulting in 341 nodes (Fig. 4.10(b)). The four side surfaces were each modeled by 35 elements (116 nodes). The bottom surface was modeled by 25 elements (96 nodes). The velocity of the nodes at the edge of the top plate were set to zero because clamped boundary conditions were assumed. The velocity of each point of the side plates and the bottom plate was also assumed to be zero.

The general mesh requirement for a BEM model is that the largest dimension of the elements is less than 1/4 of the acoustical wavelength. For the highest frequency in the present study, i.e., 500 Hz, this meant that the size of the mesh should be less than approximately 17 cm. The dimension of the BEM mesh for the measured vibration in the present study was about 5 cm. The largest dimension of the BEM model for the FEM-

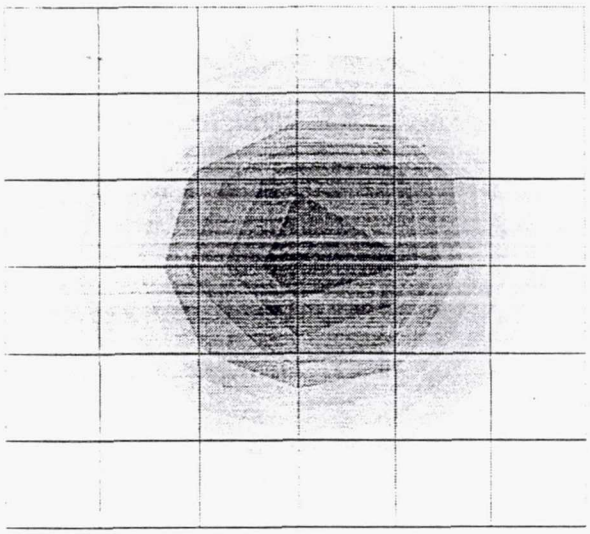

(a)

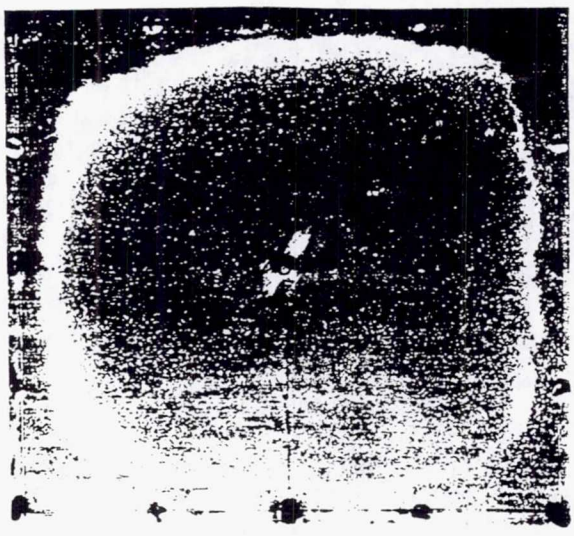

(b)

Figure 4.9 Comparison of predicted and measured modes of the plate: (a) first mode, FEM, (b) first mode, experimental, (c) second mode, FEM, (d) second mode, experimental.

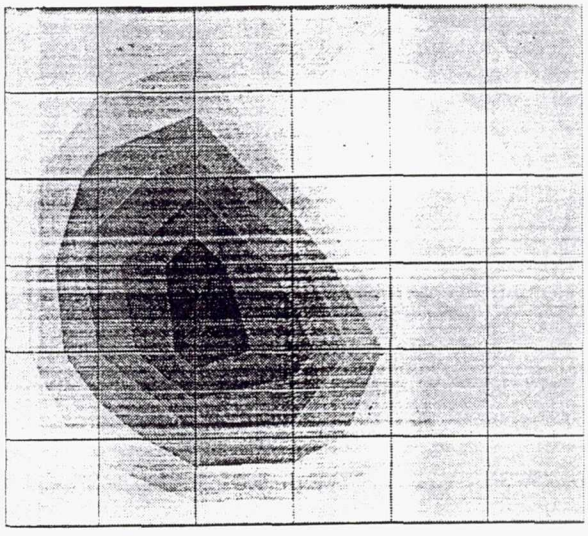

(c)

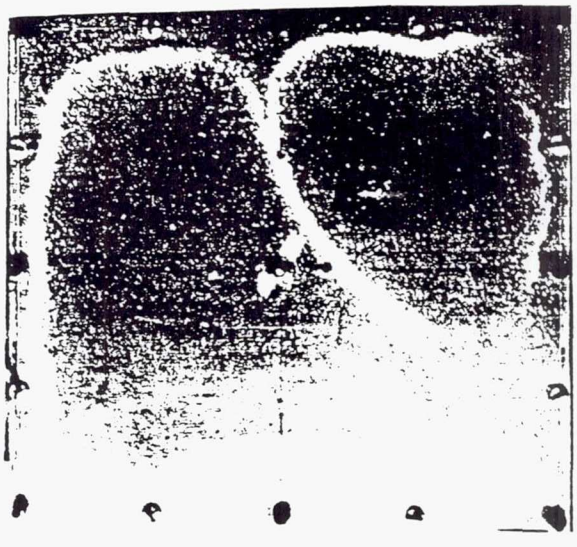

(d)

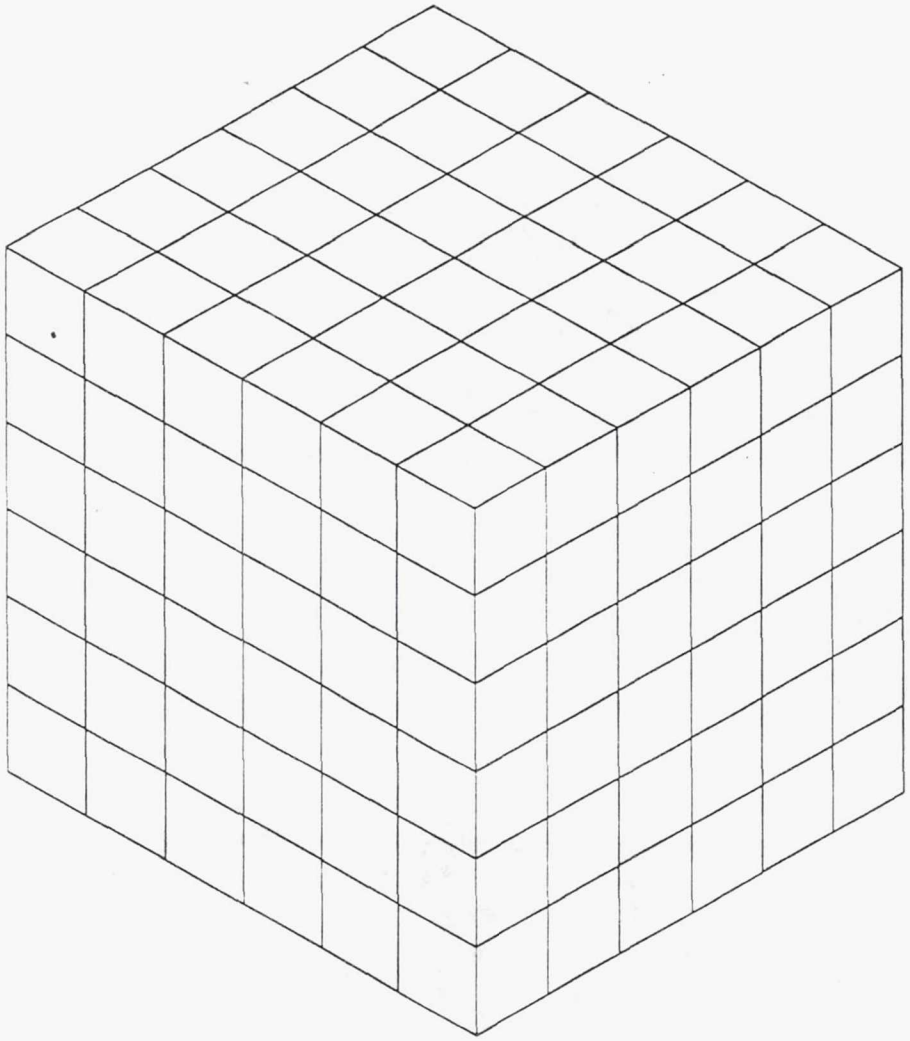

Figure 4.10(a) BEM model for measured vibration.

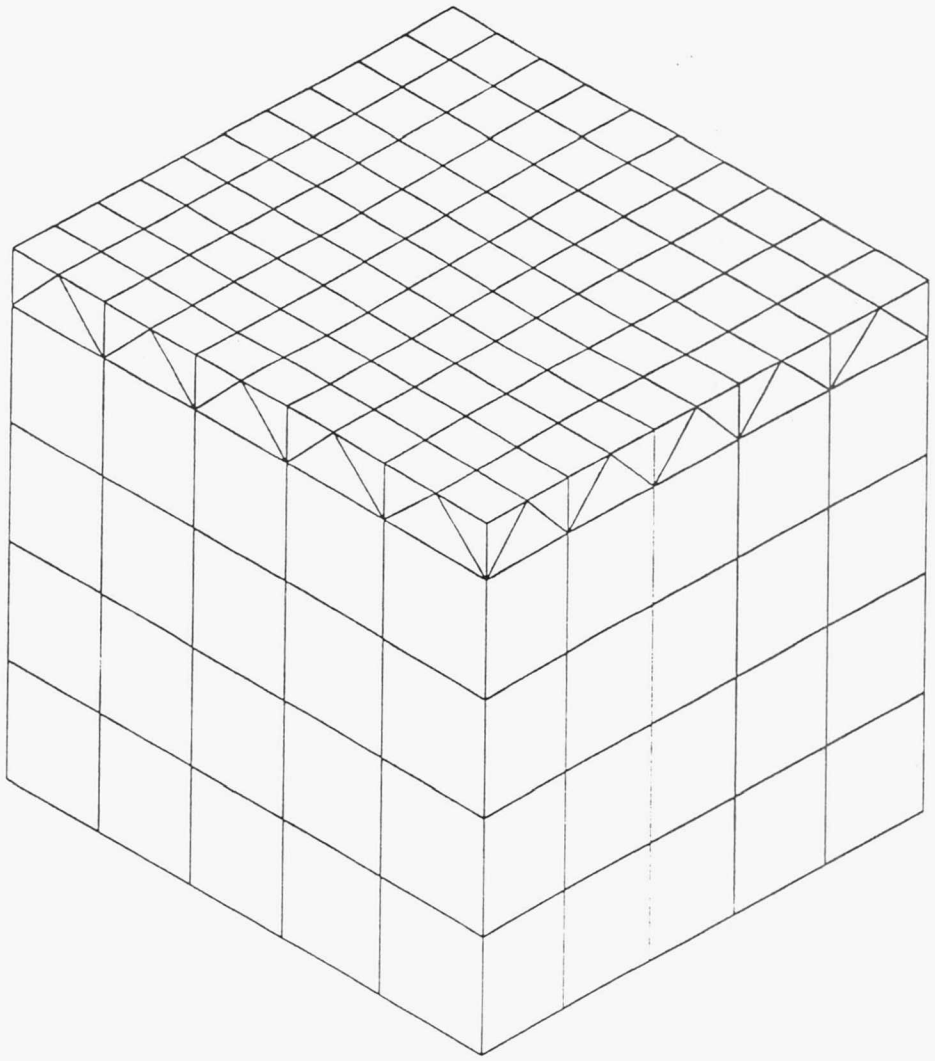

Figure 4.10(b) BEM model for FEM predicted vibration.

predicted vibration was about 6 cm. Therefore, both BEM models were unnecessarily fine for the acoustical analysis. However, in the present study, the BEM mesh was made considerably finer to assure compatibility with the FEM mesh and the vibration measurement grid.

4.5 Results

Three kinds of results were obtained: measured sound power, numerical prediction of sound power, and prediction of sound power from measured vibration (Fig.4.11).

Table 4.2 shows the peak values of three kinds of results mentioned above. Since a number of intensity measurements were made, averaged values and their ranges were given as the measured sound power levels. The measured sound power levels in Fig. 4.12 and Fig. 4.13 which will be discussed later in this chapter are two examples of the measurements.

To validate the acoustic portion of the model, measured vibration data was used in the BEM model shown in Fig. 4.10(a). The total radiated sound power was also measured using the sound intensity method. The results are compared in Fig. 4.12. The shape of the measured and predicted sound power traces are very similar but the measured sound power is generally slightly greater than predicted values.

The experimental data far below the peaks, i.e., the data below 90 dB, are not smooth and are generally higher than predicted values. There are three expected sources of error which will be most significant below the resonance peaks and which limit the dynamic range of the results: 1) In the BEM model we have assumed zero vibration from the sides of the box. Since the sides are much stiffer than the top and since the excitation is directly applied to the top rather than the sides, this is not a bad assumption. However there will still be some vibration and hence sound radiation from the sides. This will make BEM underestimate the noise radiation from the box. Also, since the sides will have their own modes of vibration, the measured sound trace will reflect these modes. This may account for the nonsmooth character of the measured sound below the four resonant peaks. 2) Vibration data at the edge nodes of the mesh were set to zero (to agree with the clamped boundary conditions of the FEM model) while the actual box will have some motion at the edges. 3) Phase mismatch in the microphones used in the intensity probe introduces a residual intensity error which may become significant for frequencies at which the measured intensity is very low.

The second, third and fourth peaks of the experimental curve in Fig. 4.12 are shifted slightly to the right. The reason for this shift is that the two measurements, vibration and sound intensity, were not made at the same time. In fact, the vibration measurements were obtained over a four-hour period. The system changed somewhat during the measurements.

Figure 4.13 shows the total radiated sound power obtained by measurement (i.e., same as in Fig. 4.12), and that obtained by using the FEM and the BEM model in Fig. 10(b). Except for a shift in the resonance frequencies (due to the FEM model, see Fig. 4.8), the combined FEM/BEM model yields a good prediction of the radiated noise.

The data in Figs. 4.12 and 4.13 are plotted in one-third octave bands in Fig. 4.14. The trends in the data are the same, with the greatest difference occurring in the 100 Hz one-third octave band. The likely reason for this is that the measurement of sound intensity at low frequencies is less accurate than at higher frequencies.

Table 4.2 Comparison of Sound Power Level of Four Peak Values

	Mode 1	Mode 2	Mode 3	Mode 4
Measurements	113±0.5 dB	111±1 dB	107.5±0.5 dB	109.5±0.5 dB
BEM/Measurements	109 dB	106.5 dB	109 dB	103.5 dB
BEM/FEM	111.5 dB	108 dB	104 dB	103.5 dB

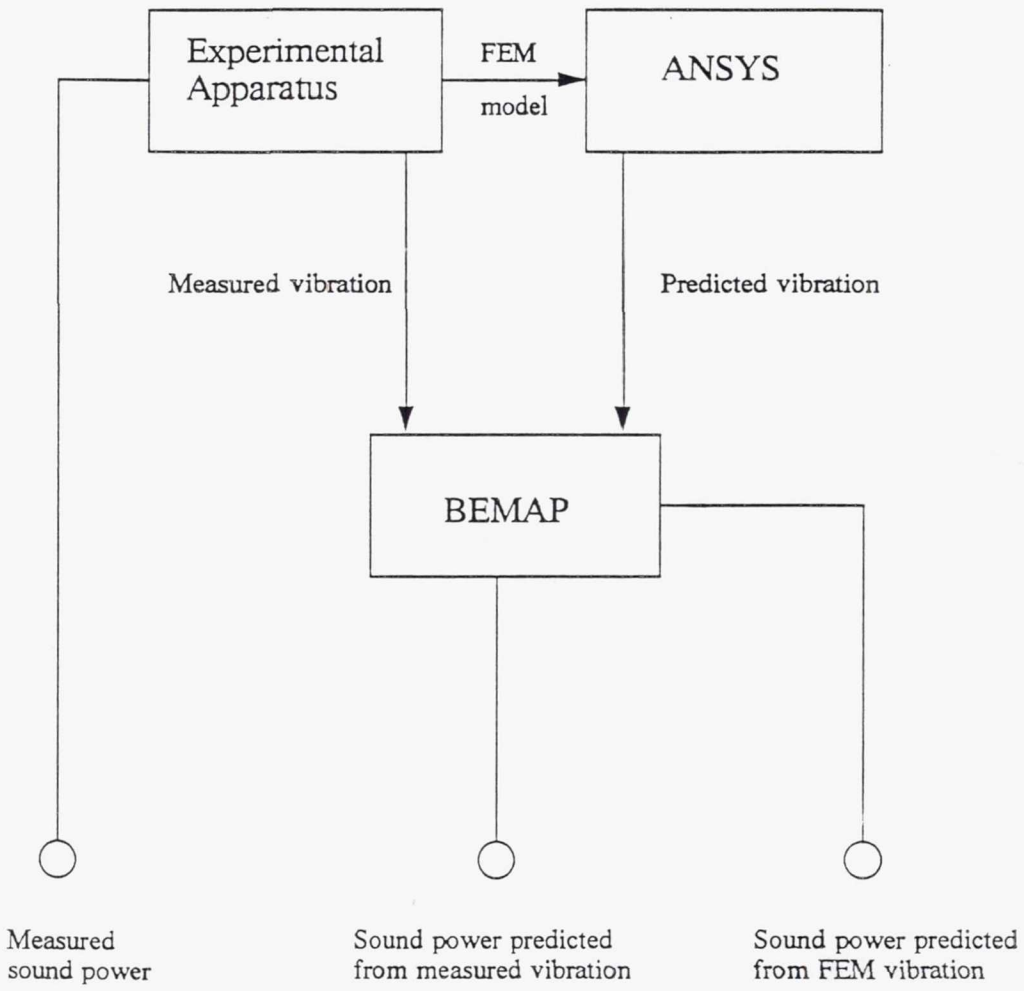

Figure 4.11 Flow chart for the results .

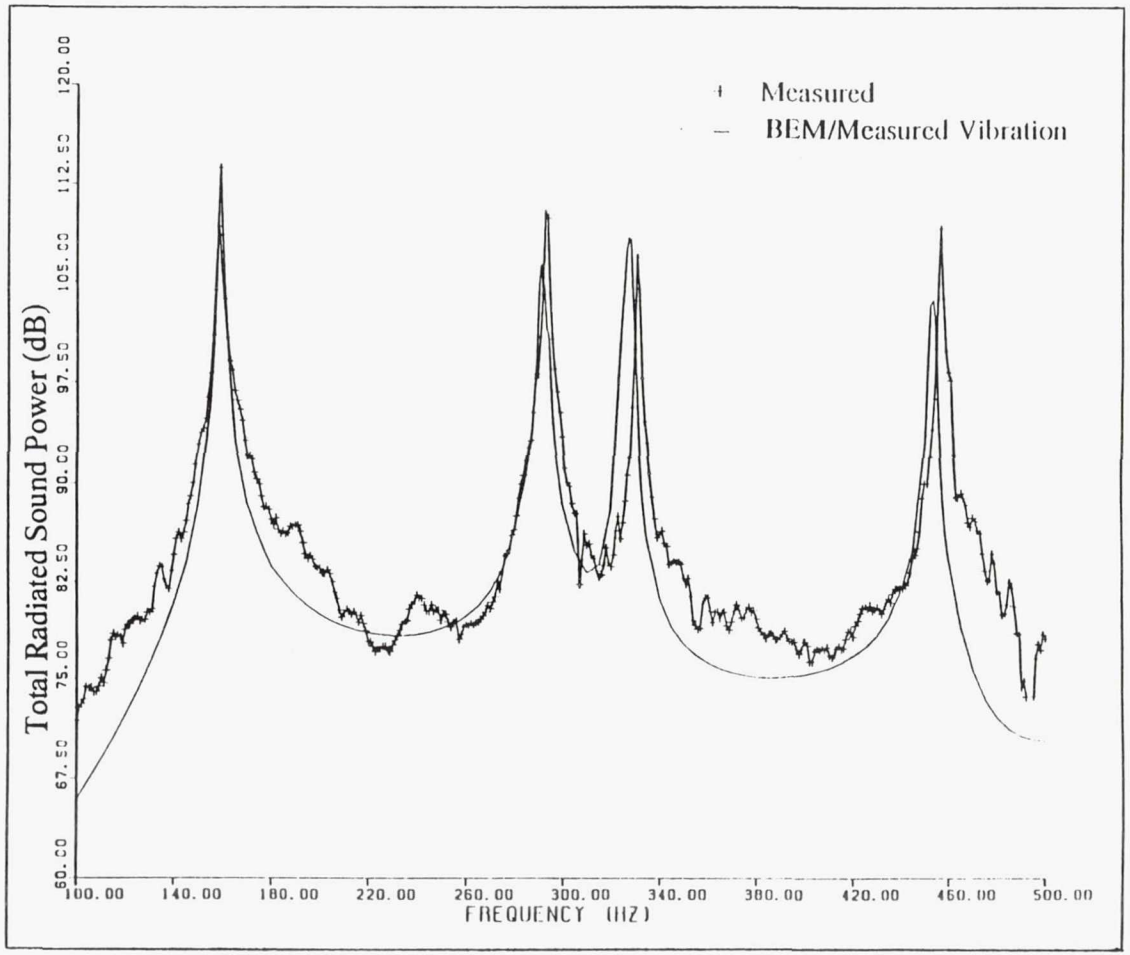

Figure 4.12 Total radiated sound power from measurement and predicted from measured vibration.

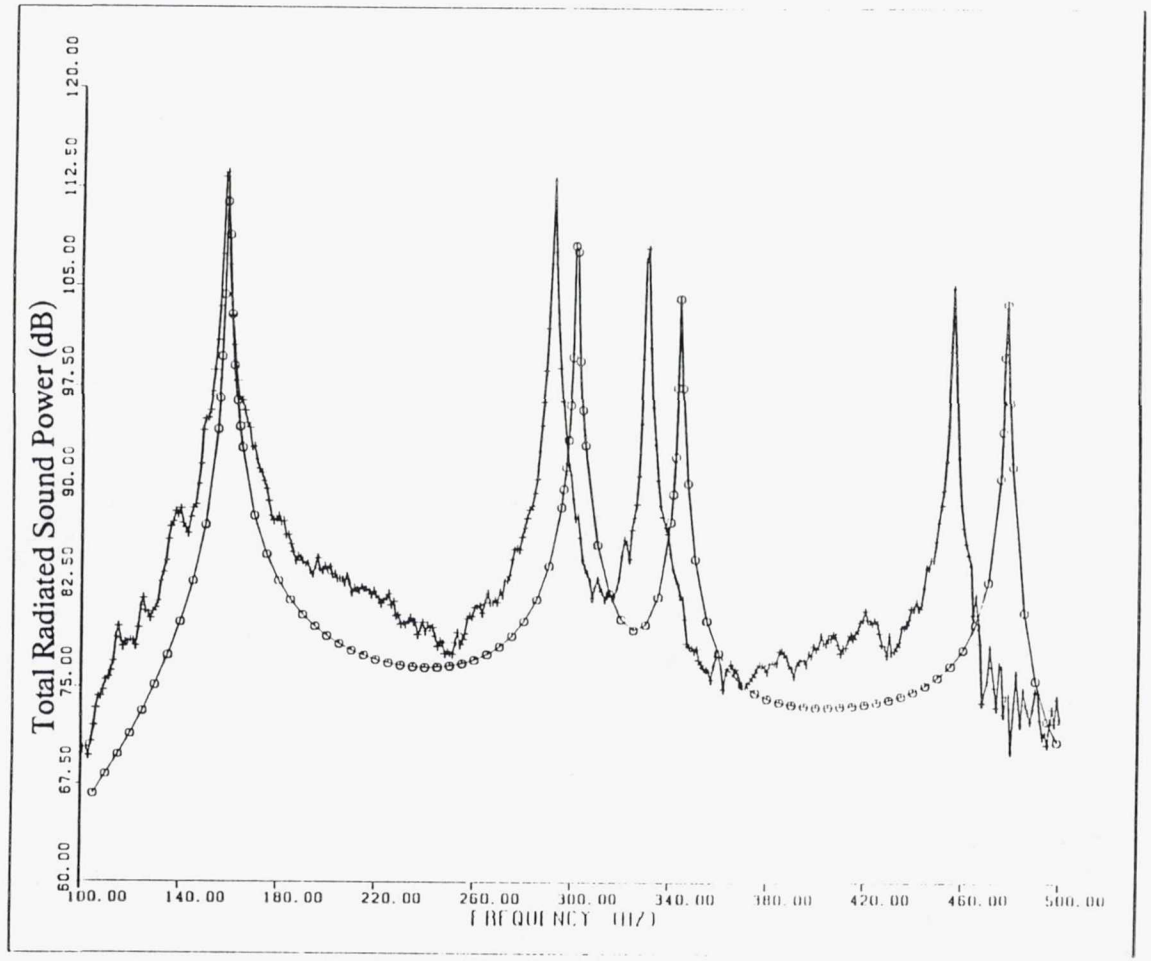

Figure 4.13 Total radiated sound power from measurement and predicted from FEM vibration.

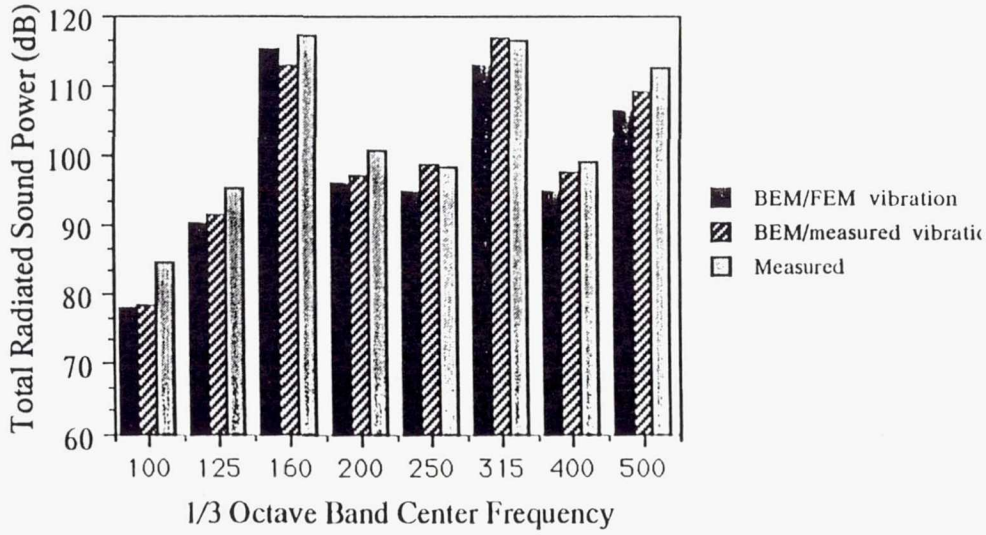

Figure 4.14 One third octave band for sound power.

Table 4.3 Linear and A-weighted Total Radiated Sound Power Level in the Frequency Range 100-500 Hz

	Linear	A-Weighted
Sound Power From Experiment	120.5 (dB)	113.5 (dB)
Sound Power Predicted from FEM Vibration	118.0 (dB)	109.5 (dB)
Sound Power Predicted From Measured Vibration	119.0 (dB)	112.0 (dB)

Table 4.3 shows the total radiated sound power, both Linear and A-weighted, in the frequency range 100-500 Hz. The measured sound power has the highest value, and the combined FEM/BEM prediction yields the lowest value, with a difference of 2.5 dB and 4 dB respectively, in linear and A-weighted senses. The four side surfaces are vibrating slightly and therefore radiate sound when the top plate is excited by the shaker, but only the motion of the top plate is included in the BEM model. Consequently, the BEM models underestimate the true sound power.

4.6 Summary and Conclusions

Analytical and experimental methods were used to validate the predictions of the boundary element method (BEM) acoustic computer code BEMAP. A finite element method (FEM) study was performed to predict the vibration of a simple rectangular box. Vibration measurements were compared with the FEM predictions. Sound power radiation from the box was predicted based on both the predicted and measured vibration. Sound power predictions were compared to measured values. The results show that:

1) Numerical techniques such as the FEM and the BEM may be used to predict radiated noise accurately.

2) Discrepancies between measured and predicted sound power are due to errors in the FEM model, error in the measurement of sound power and error in the measurement of vibration.

CHAPTER 5

THE EFFECT OF STIFFENING BY ADDING A RIB TO THE STRUCTURE

5.1 Introduction

A natural extension of the researech discussed in the Chapter 4 is the study of ribbed structures. Ribbed structures have many practical applications in engineering. One major advantage of a ribbed structure is that they can enhance the strength or improve the thermal characterictics of the structure, without increasing the weight significantly. They are therefore commonly used on enclosures and as structural members of machinery.

Maidanik conducted an analysis of a ribbed panel under acoustical loading [49]. His work was based on the assumption of equipartition of modal energy. On that basis, he estimated the radiation efficiency of the panels under acoustic loading. He found that ribbing increased the radiation efficiency of the panel and hence its coupling to the acoustic field. The results were validated by experimentation. The agreement between theory and experiments was shown to be satisfactory.

If a structure is under a specific loading, either acoustic or mechanical, the vibrational pattern of the structure usually does not satisfy the assumption of equipartition. Thus most of the problems encountered may not be solved by the methods used in Ref. [49]. In these cases, finite element and boundary element methods provide a better way.

The numerical and experimental methods used in the study of ribbed structures are the same as those used for unribbed structures, as described in Chapter 4. First, finite element models were constructed for ribbed structures. Before these models were used to predict structural vibration, they were validated by experiments. The boundary element method was then used to predict radiated noise from the FEM predicted vibration. The sound intensity method was used to measure the total radiated sound power in order to validate the predicted radiated noise.

The total radiated sound power of a vibrating structure is proportional to the radiation efficiency and the space averaged mean square velocity of the structure. Ribbing increases the radiation efficiency, but on the other hand, reduces the amplitude of the mean square velocity. The change of the total radiated sound power is determined by what change is dominant: the increase of the radiation efficiency, or the decrease of the vibration level.

Three cases were studied as shown in Fig. 5.1. The dimension of the cross section of the rib was 1/4 inch × 1/4 inch (Fig. 5.2). The length of the ribs varied, depending on the position of the ribs. For position (1), the length of the rib was 14.15 inches; for position (2), the length was 9.90 inches; and for position (3), the length was 10.80 inches. The ribs were made of aluminum, the same material as that for the top plate of the structure. In all three cases, the ribs were bolted to the top plate of the structure.

5.2 FEM and BEM Models

Finite element models were constructed for all three cases. The FEM models for the ribbed structures were combinations of the FEM model used for unribbed structure, as described in Sec. 4.4.1, and the FEM model for the rib. In the FEM, the element used was a 3-D tapered unsymmetrical beam. One characteristic of this element is that it can define

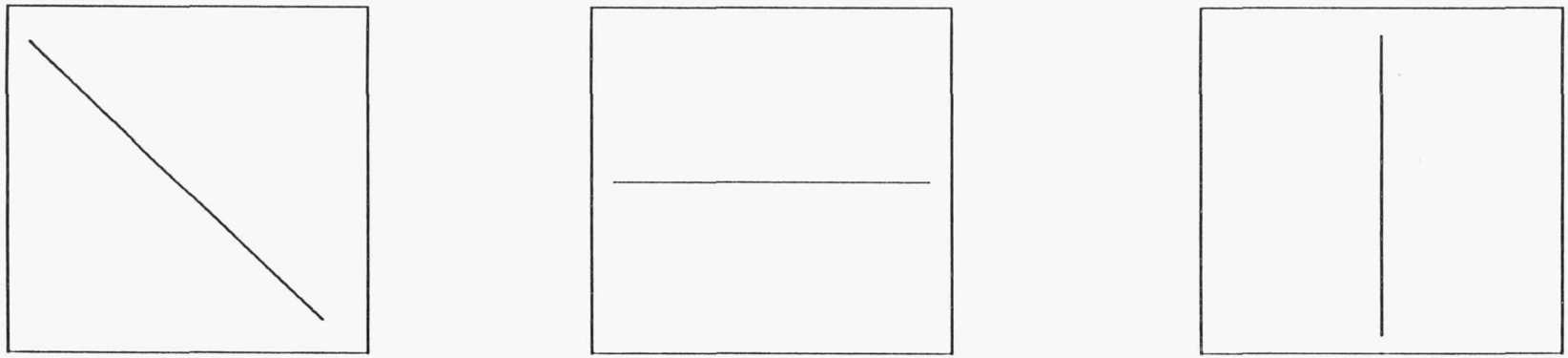

Figure 5.1 Position of ribs.

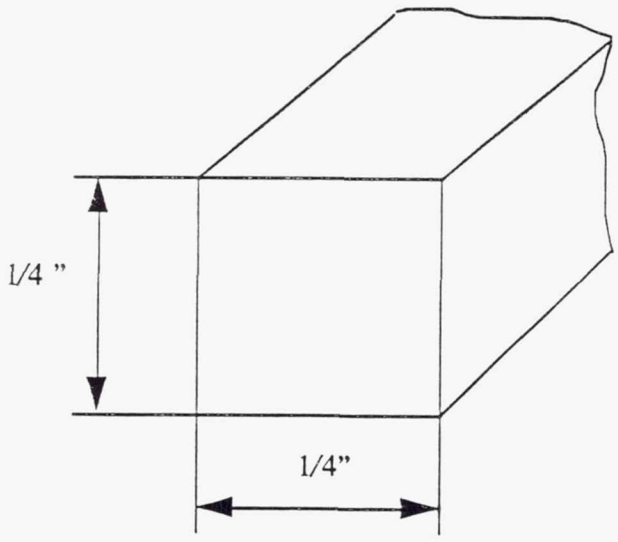

Figure 5.2 Dimension of ribs.

an offset constant of the centroid location of the section relative to the nodal point location. In the present study, the nodal points were on the top plate with an offset of 1/8 inch, as shown in Fig. 5.3.

Boundary element models used for the ribbed structures were the same as those used for unribbed structures, as described in section 4.4.2. The BEM models were used to predict sound intensity and total radiated sound power.

5.3 Vibration

The vibration level of the ribbed structures was studied by the FEM. Again, the commercial FEM code ANSYS was used to calculate the response of the system being excited by a unit amplitude force applied to the top plate. A clamped boundary condition was applied to the edges of the plate. Figure 5.4 shows the space averaged mean square velocity of the four different cases. Since ribbing stiffened the structure, the resonance frequencies of ribbed structures were pushed higher. On the other hand, it is not clear from Fig. 5.4 if the overall level of the mean square velocity of the structures in the frequency range 100-500 Hz decreases. But if the average over the frequency range is taken, as shown in Table 5.1, it is apparent that ribbing decreases the vibrational level of the structure.

Measurements of the vibration were also performed. Since the purpose of the measurement at this point was only to validate the FEM model, only a few points were selected for the measurement. The measured frequency response functions (FRFs) were compared with the FEM calculated FRFs. Figures 5.5 and 5.6 are the drive point frequency response functions for two different cases. Like the unribbed structure, the major discrepancy shown in the figures is the shift of natural frequencies.

5.4 Radiation Efficiency and Total Radiated Sound Power

Using the vibration data calculated by FEM, the radiation efficiency and total radiated sound power of the ribbed structures were computed by BEMAP. Figure 5.7 shows the radiation efficiency of four different cases. One is for an unribbed structure, and the other three are for ribbed structures with the rib at three positions. It is clear that ribbing increases the radiation efficiency. Although the radiation efficiency of ribbed structures is less than that of the unribbed structure at some frequencies, the overall level of the radiation efficiency in the frequency range increases.

Figure 5.8 shows the total radiated sound power of the four different cases. Like the space averaged mean square velocity, the peaks of the total radiated sound power of the ribbed structures were pushed to higher frequencies. The amplitudes of the first resonance are almost the same for each of the four different cases. For the second and the third peaks, the ribbed structures have much higher amplitudes, which will contribute significantly to the total radiated sound power in the frequency range 100-500 Hz. Table 5.2 shows the total radiated sound power in the frequency range 100-500 Hz. It is noted that the increase of A-weighted total radiated sound power is larger than that of the linear total radiated sound power. This indicates that the high frequency content increased in the noise radiated by ribbed structures. This is in accordance with the fact that ribbing increases the resonant frequencies.

The validity of the BEM predicted sound power was checked by experimentation. The sound intensity method was used to measure the total radiated sound power. The sweeping technique was used in the SIM. The steel rod frame that was used previously for the unribbed structure was used to define the sweeping surface. Figs. 5.9 and 5.10 are

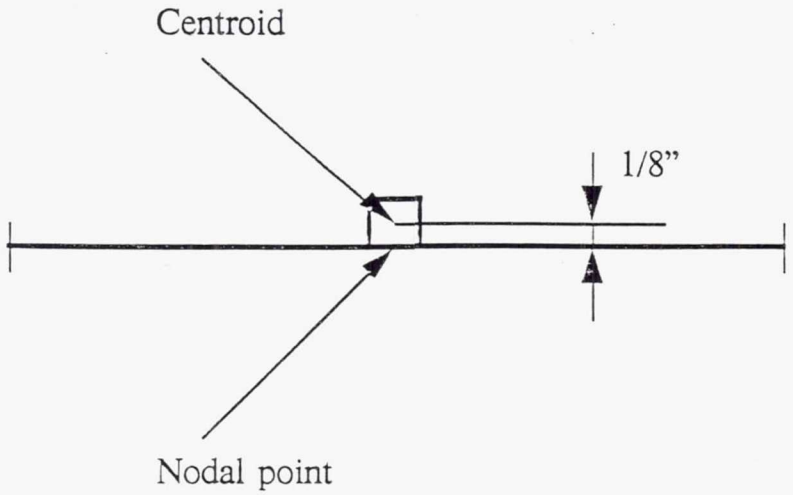

Figure 5.3 Relative position of the centroid and the nodal point of the beam.

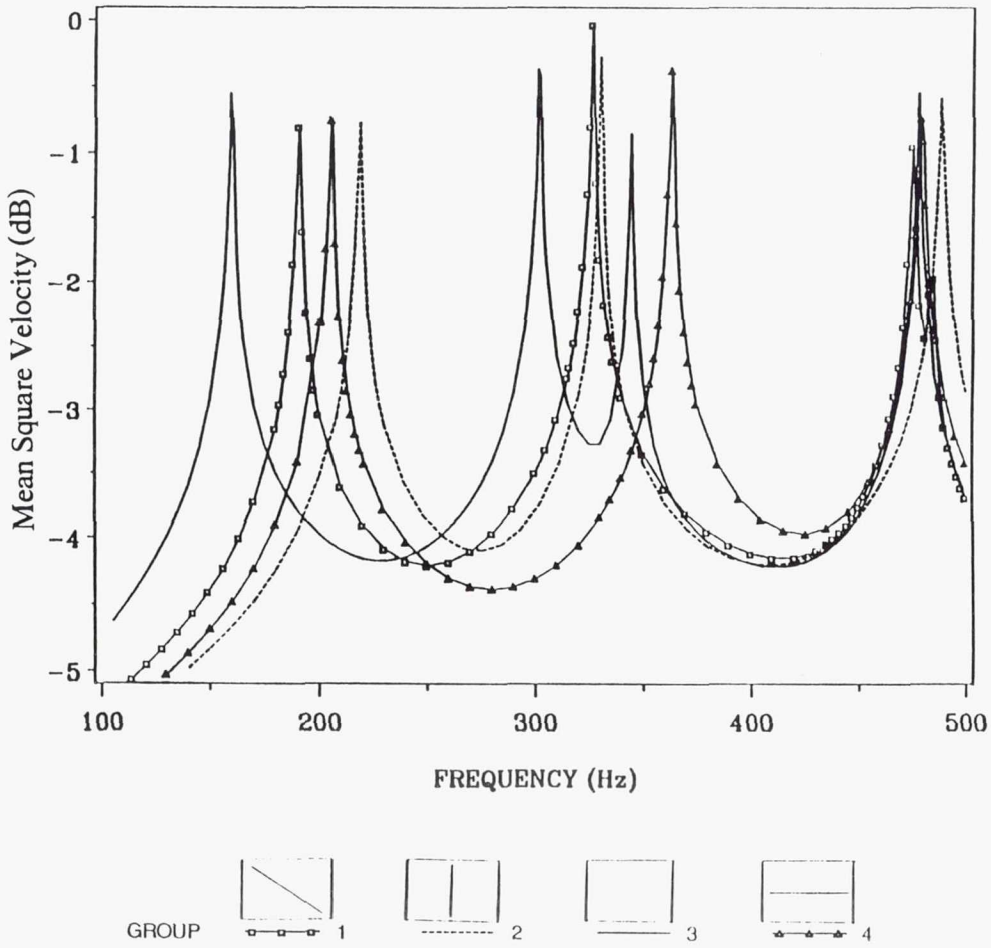

Figure 5.4 Space averaged mean square velocity for four cases.

Table 5.1 Mean Square Velocity Averaged in the Frequency Range 100-500 Hz.

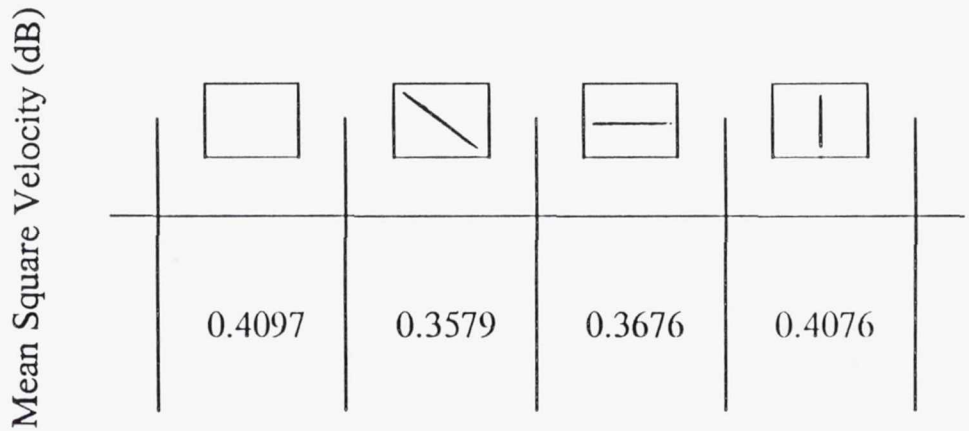

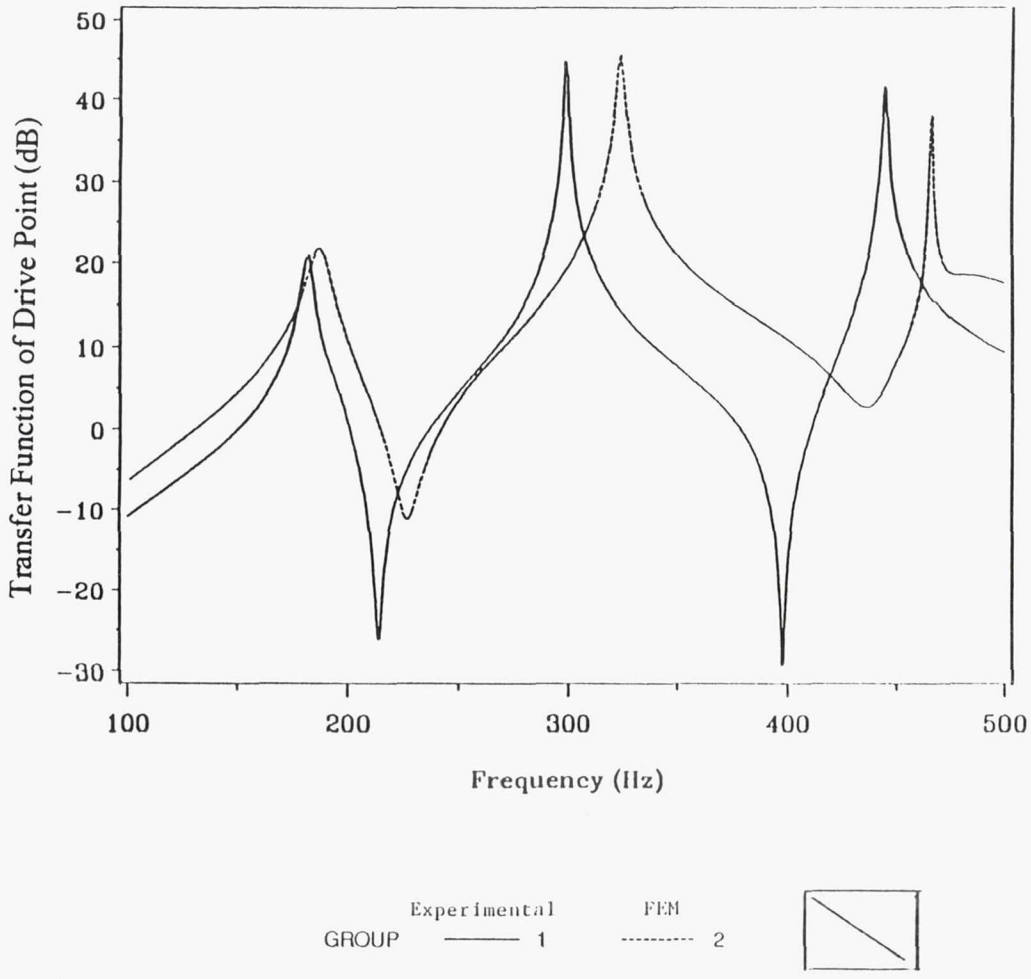

Figure 5.5 Frequency response functions from measurement and FEM for the shown rib position.

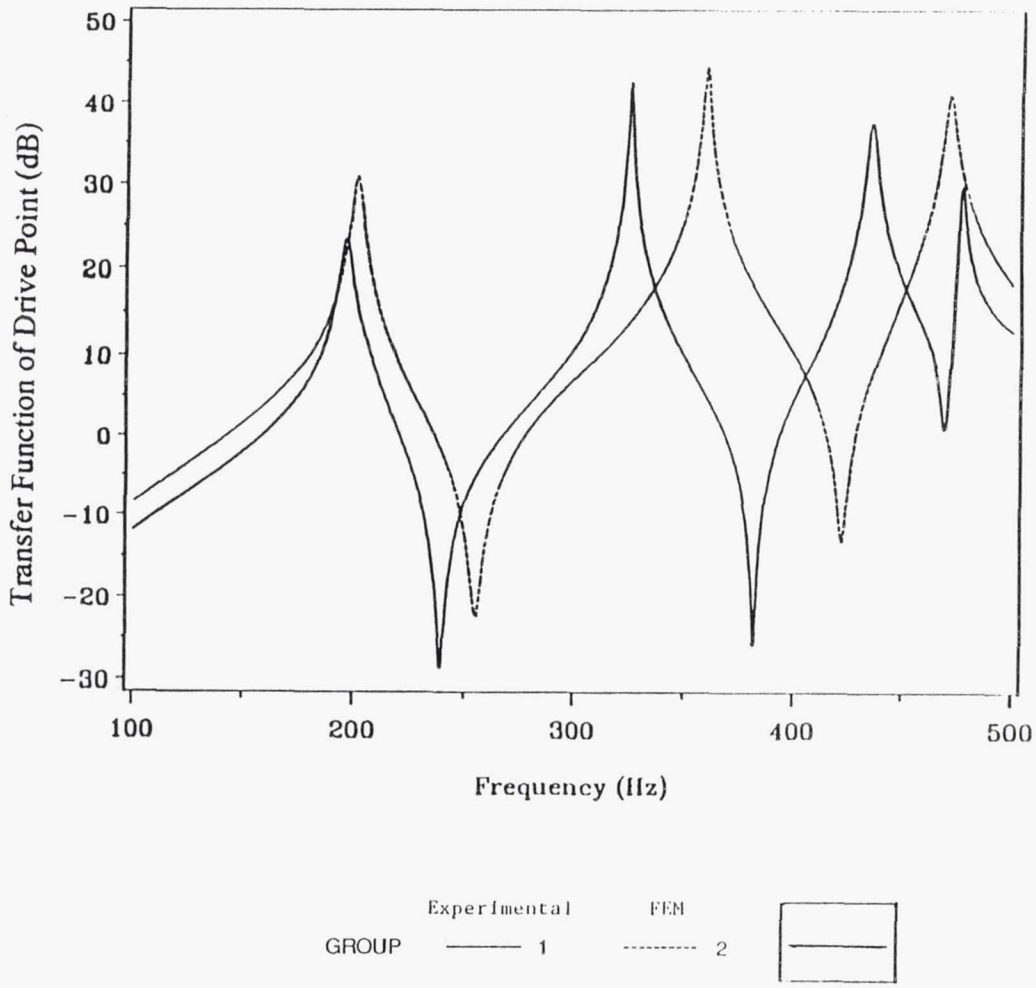

Figure 5.6 Frequency response functions from measurement and FEM for the shown rib position.

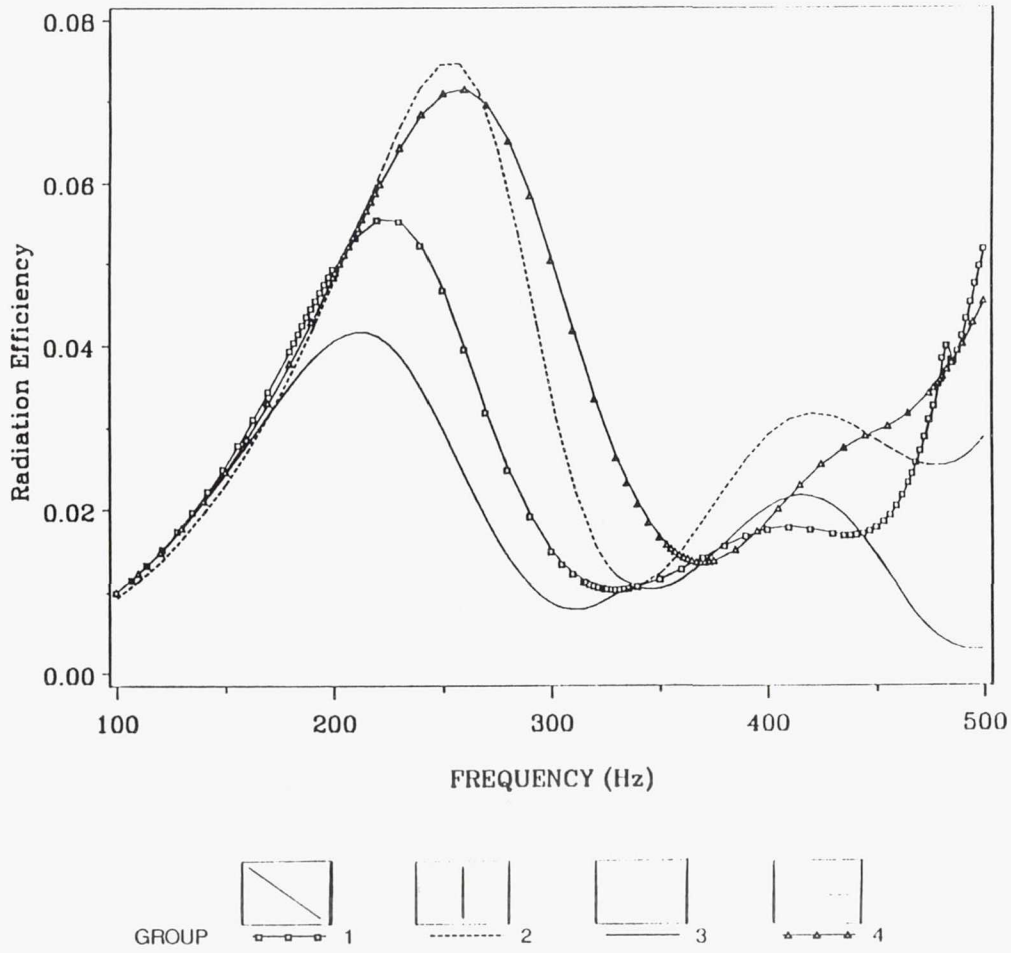

Figure 5.7 Radiation efficiency for four different cases in the frequency range 100-500 Hz.

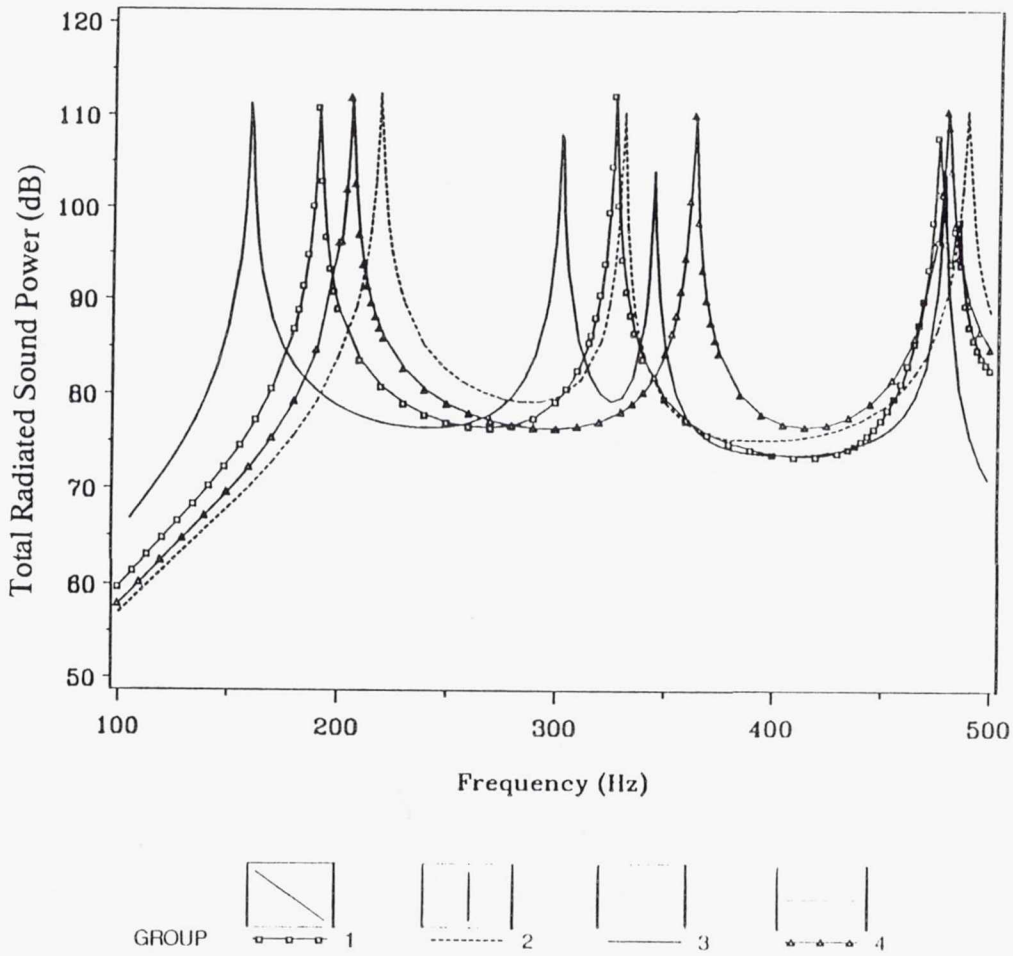

Figure 5.8 Total radiated sound power for four different cases in the frequency range 100-500 Hz .

Table 5.2 Linear and A-weighted Total Radiated Sound Power Level from FEM/BEM (dB)

	Linear	A-Weighted
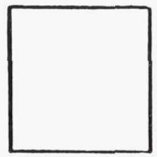	118.0	109.5
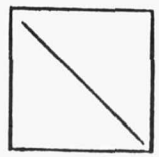	119.0	113.0
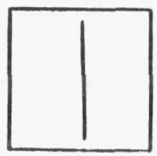	120.5	114.5
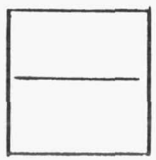	120.5	115.0

comparisons of the measured to the predicted total radiated sound power for two different cases. Since it is more difficult to model ribbed structures, the differences between the predicted and measured results in Figs. 5.9 and 5.10 are greater than that in Fig. 4.13.

In the frequency range 100-500 Hz, the total radiated sound power for two cases was summed to obtain both linear and A-weighted sound power levels. The results are compared to the total radiated sound power of the structure without the rib, as shown in Table 5.3. The numbers in Table 5.3 confirm that ribbing increases the total radiated sound power as well as the high frequency content.

5.5 Discussion

For a simply supported plate vibrating at a flexural mode, when the frequency is such that the acoustic wavelength exceeds the structural vibration wavelength in both the long and short dimensions of the plate, i.e., $ka < m\pi$, and $kb < n\pi$, the maximum value of intensity is [50]

$$I_{max} = 2\rho_0 c\,|V_{mn}|^2 \left(\frac{kab}{\pi^3 rmn}\right), \tag{5.1}$$

where V_{mn} is an amplitude coefficient and m and n are integers. Now consider a single modal cell of area ab/mn in the absence of any other surface motion. Since the dimension of the cell has been assumed to be much smaller than an acoustic wavelength, the single cell may be modeled by a point source of volume velocity given by

$$\begin{aligned} Q &= 2\,V_{mn} \int_0^{a/m} \int_0^{b/n} \sin(m\pi x/a)\sin(n\pi z/b)\,dx\,dz \\ &= V_{mn}\,(8ab/\pi^2 mn), \end{aligned} \tag{5.2}$$

Then, the farfield intensity at all points a distance, r, from the source is

$$I = \frac{|P(r)|^2}{2\rho_0 c} = 2\rho_0 c\,|V_{mn}|^2 \left(\frac{kab}{\pi^3 rmn}\right)^2, \tag{5.3}$$

where P(r) is calculated from [51]

$$P(r,t) = j\omega\rho_0 \frac{Q}{4\pi r}\,\exp[j(\omega t - kr)]. \tag{5.4}$$

By comparing Eqs. (5.1) and (5.3) it is noted that the intensity that would be produced by one cell equals the maximum intensity generated by all the mn cells acting together. Because the intensity produced by one cell is independent of position, whereas

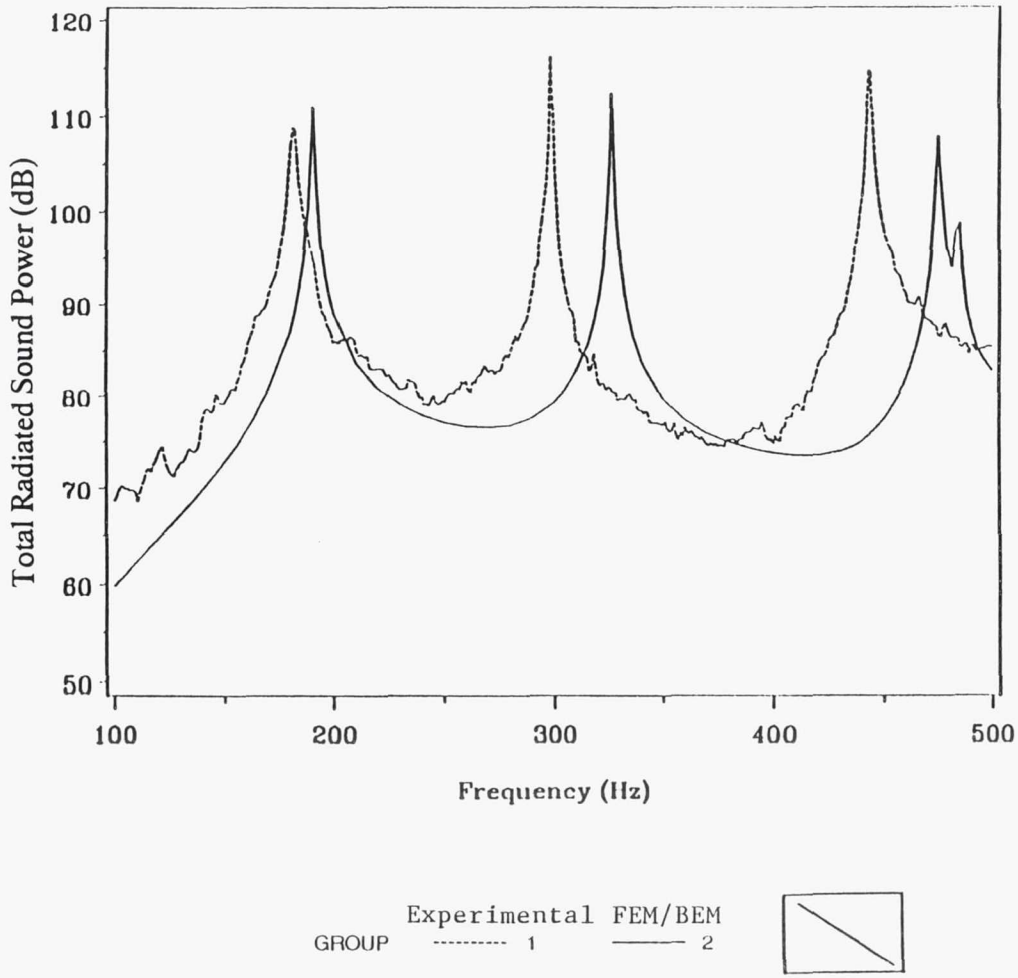

Figure 5.9 Total radiated sound power from measurements and FEM/BEM for the shown rib position.

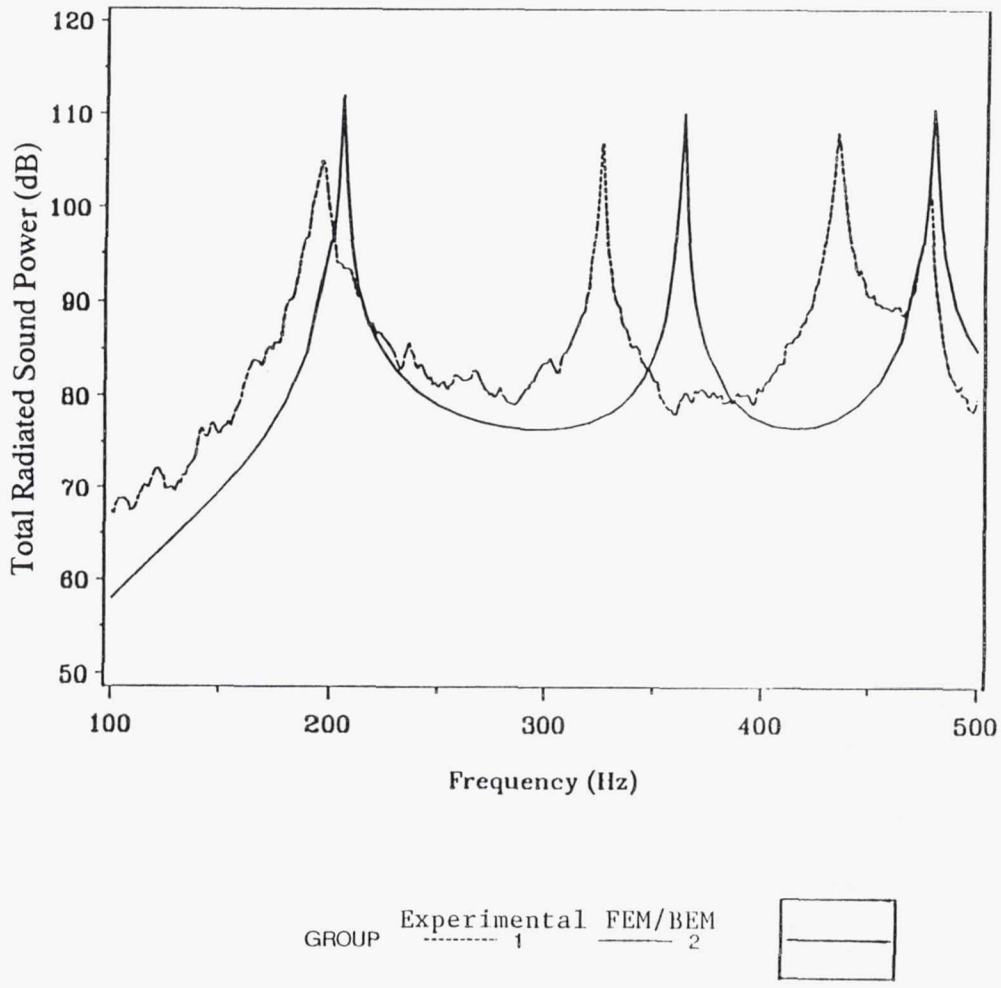

Figure 5.10 Total radiated sound power from measurements and FEM/BEM for the shown rib position.

Table 5.3 Linear and A-weighted Total Radiated Sound Power Level from Measurement.(dB)

	Linear	A-Weighted
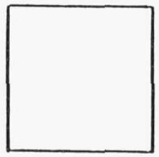	120.5	113.5
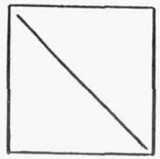	121.0	117.0
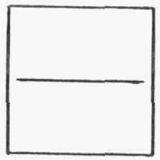	121.5	116.5

the intensity produced by the complete panel is less in all other directions than the maximum given by Eq. 5.1, the total sound power radiated by a single isolated cell would exceed that radiated by the whole panel.

It can also be proven that the radiation efficiency of all panel modes at low frequencies is at most equal to, and mostly less than, that corresponding to the isolated cell vibration [50].

When ribs are attached to a panel, the panel is divided into many small panels, and therefore the total radiated sound power and the radiation efficiency are increased. In fact, for a simply supported panel under acoustical loading, the radiation efficiency at low frequencies is increased by a factor of $(2P_{rib} + P)/P$, where P_{rib} is the total length of the rib and P the length of the panel perimeter [49].

In the present study, the same BEM model was used for the calculation of total radiated sound power and radiation efficiency of both ribbed and unribbed structures, i.e., the geometry change of the structure was not included in the BEM model. The difference of the BEM models between ribbed and unribbed structures was in the input data. This indicates that the distribution of the normal velocity or displacement of the panel plays a very important role in determining the radiation efficiency and total radiated sound power.

Consider the idealized case presented in Fig. 5.11, which illustrates a one-dimensional vibration. The panel is vibrating sinusoidally. This means that adjacent internodal cells have volume velocities of equal magnitude and opposite sign, so that they actually cancel each other's ability to radiate sound. Consequently, only the half cells at the corners remain. Any distortion from the sinusoidal form, by attachment of a support or ribs, will affect this cancellation, thus increasing the radiation efficiency. This reasoning can be extended to the real two-dimensional case to provide a physical explanation of the increase of the radiation efficiency by adding ribs to structures.

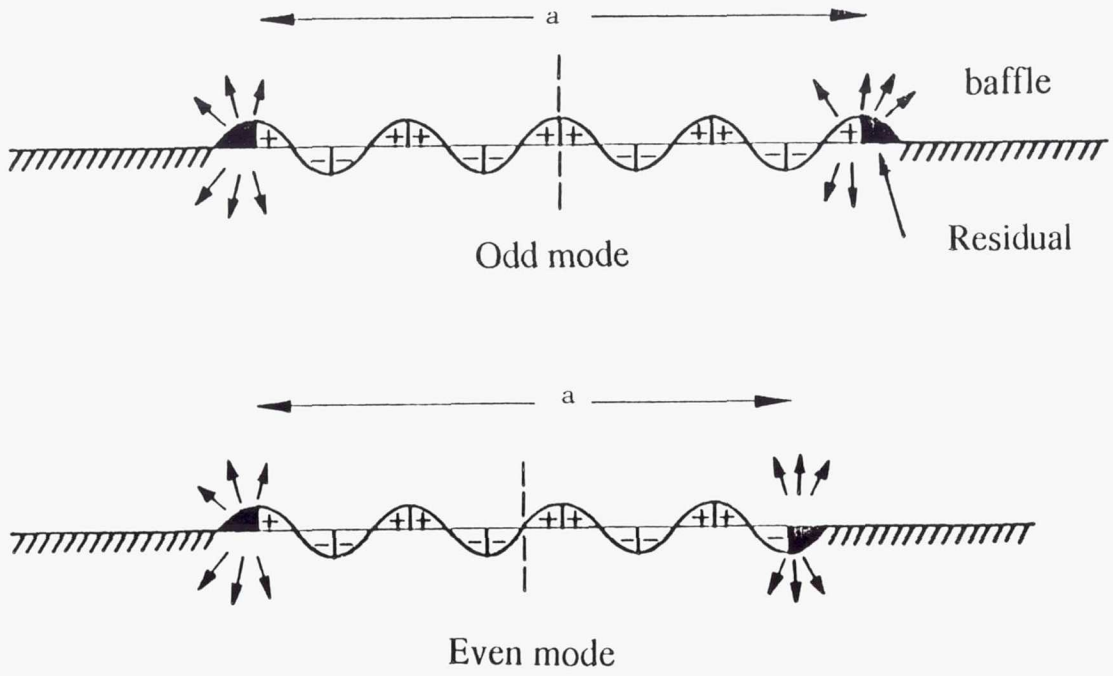

Figure 5.11 Intercell cancellation on vibrating plates .

CHAPTER 6

SUMMARY, CONCLUSION AND SUGGESTION FOR FUTURE RESEARCH

A combined numerical and experimental validation of methods was used to predict structural vibration and radiated noise. The finite element method (FEM) was used to predict structural vibration. The modal superposition method was used in the FEM to perform modal analysis and to calculate system response. Experimental modal analysis was used to validate the FEM results. The validation included three parts: validation of natural frequencies, validation of mode shapes, and validation of frequency response functions.

The boundary element method (BEM) was used to predict radiated noise. The prediction was based on both predicted and measured vibration data. In order to approximate the situation in which the experimental apparatus was sitting on the floor, a modified Helmholtz integral equation for bodies sitting on an infinite plane was used in the present study.

Although the BEM is a very efficient numerical technique for acoustic analysis for a single frequency, it may lose its advantage for a multifrequency run. In this research, a frequency interpolation technique was implemented in the BEM code BEMAP. By using this technique, the BEM retained its advantage for multifrequency acoustic analysis.

The sound intensity method was used to verify the predicted noise radiated by the structure. Because sound pressure produced by a source depends not only on the sound energy radiated by the source, but also on the environment in which the source is located and the relative position of the microphone and the source, it is not an adequate means to characterize a noise source. On the other hand, sound power of the source is the rate at which the source radiates sound power, thus it is a more meaningful quantity to use in characterizing a noise source. By using the sound intensity method, sound power can be determined by integrating the intensity over the surface that encloses the noise source.

In the sound intensity method, there are two factors that would affect the accuracy of measurements and thus determining the measurement frequency range. One factor is the high frequency finite difference error, the other is the low frequency microphone phase mismatch error. By choosing proper spacing between microphones, the high frequency finite difference error can be minimized. In order to eliminate the microphone phase mismatch error at low frequencies, a phase correction scheme was implemented. In this research, a specially designed equipment was used to measure the microphone phase mismatch, and was used to correct the measured phase angle between the two signals from two microphones.

The numerical/experimental results show that numerical techniques such as the finite element method and the boundary element method may be used to accurately predict structural vibration and radiated noise. There are several error sources that may cause discrepancies between predicted structural vibration and radiated noise, and those derived by actual measurements. The sources of error include error in the FEM model, error in the measurement of sound power, and error in the measurement of vibration. If the vibration data (either measured or supplied by the FEM) are reliable, the acoustic BEM will yield accurate results for the predicted sound power.

For structures with ribs, the space averaged mean square velocity is reduced since the system becomes more rigid after the ribs are attached. On the other hand, since ribbing

damages the cancellation of internodal cells' ability to radiate sound, the radiation efficiency of ribbed structures is higher than that of unribbed structures. The increase of radiation efficiency usually offsets any decrease in the mean square velocity. Therefore, the total radiated sound power of ribbed structures is higher than that of the unribbed structures.

Although good results have been shown herein for structures with relatively simple geometries, the methodology used in this study can be extended to structures having complex shapes. In fact, the primary utility of the present study is in its capability to investigate more general problems involving any arbitrarily shaped structures.

Although several aspects in this area have been investigated, there are many more that remain to be explored. For example, coupling between structure and fluid is not considered in the present study, since compared with mechanical excitation, the acoustic loading is negligible. For a very thin plate under relatively weak excitation, or in case where the acoustic medium is more dense, e.g., sea water, the coupling effect between structure and acoustic medium may need to be considered.

The methodology used in this research may also be extended to the study of vibration and radiated noise in structures with openings. In the boundary element method, there are usually two ways to handle the problem of structures with openings. The first is to estimate the impedance at the openings, and then use the regular BEM. If this method is used, the accuracy of estimation of the impedance is essential to the accuracy of the solutions, especially those in an area close to an opening. The solutions at farfield are usually not very sensitive to the estimation of the impedance.

The second way to handle the problems posed by structures with openings is the multidomain boundary element technique (MDB). In the MDB, the openings are considered as interfaces. The pressure and velocity potential at interfaces are solved simultaneously by solving the system equation. The advantage of MDB is that the unknowns at the openings can be solved accurately. However, when compared with the first method, MDB takes much more CPU time.

REFERENCES

1. J. J. Coy, R. F. Handschuh and D. G. Lewicki, "Identification and Proposed Control of Helicopter Transmission Noise at the Source," NASA/ARMY Rotorcraft Technology Conference, NASA Ames Research Center, Moffett Field, California. NASA TM, No. 89312. March 17-19, 1987.

2. J. J. Coy and R. C. Bill, "Advanced Transmission Studies," NASA TM, No. 100867, 1988.

3. N. D. Perreira and S. Dubowsky, "Predicting Acoustical Noise Generation in Complex Mechanical Systems," ASME J. Mech. Des., Vol. 101(2), 199-209, 1979.

4. N. D. Perreira and S. Dubowsky, "Analytical Method to Predict Noise Radiation from Vibrating Machine Systems," J. Acoust. Soc. Amer., Vol. 67(2), 551-563, 1980.

5. R. J. Bernhard and S. Takeo, "A Finite Element Procedure for Design of Cavity Acoustical Treatments," J. Acoust. Soc. Amer., Vol. 83(6), 2224-2232, 1988.

6. S. H. Sung and D. J. Nefske, "A Coupled Structure - Acoustic Finite Element Model for Vehicle Interior Noise Analysis," J. Vib. Acoust. Stress Reliab., Des, Vol. 106(2), 314-318, 1984.

7. W. L. Meyer, W. A. Bell, B. T. Zinn and M. P. Stallybrass, "Boundary Integral Solutions of Three-Dimensional Acoustic Radiation Problems," J. Sound Vib., Vol. 59(2), 245-262, 1978.

8. L. G. Copley, "Integral Equation Method for Radiation from Vibrating Bodies,' J. Acoust. Soc. Am. Vol. 41(4), 807-816, 1967.

9. H. A. Schenck, "Improved Integral Formulation for Acoustic Radiation Problems," J. Acoust. Soc. Am., Vol. 44(1), 41-58, 1968.

10. D. C. Smith and R. J. Bernhard, "An Experimental Verification of Numerical Techniques Based on the Helmholtz and Rayleigh Integral Equations," Proceedings of Noise - Con 88, 615-620, 1988.

11. C. H. Oppenheimer, "Predicting the Acoustics of an Experimental machine Enclosure Using Finite Element and Boundary Element Techniques," Master's Thesis, MIT, 1986.

12. R. H. Lyon, Statistical Energy Analysis of Dynamic Systems: The Theory and Application, MIT Press, Cambridge, MA, 1975.

13. M. J. Crocker and A. J. Price, "Sound Transmission Using Statistical Energy Analysis," J. of Sound and Vibration, Vol. 9(3), 469-486, 1969.

14. V. Cole, M. J. Crocker and P. K. Raju, "Theoretical and Experimental Studies of the Noise Reduction of an Idealized Cabin Enclosure," Noise Control Engineering Journal, Vol. 20(3), 122-132, 1983.

15. W. J. Atherton, A. Pintz and D. G. Lewicki, "Automated Acoustic Intensity Measurements and the Effect of Gear Tooth Profile on Noise," NASA TM, No.100155, 1987.

16. A. F. Seybert and T. W. Wu, "Modified Helmholtz Integral Equation for Bodies Sitting on an Infinite Plane," J. Acoust. Soc. Am., Vol. 85(1), 19-23, 1989.

17. G. Chertock, "Sound Radiation from Vibrating Surfaces," J. Acoust. Soc. Am., Vol. 36(7), 1305-1313, 1964.

18. W. A. Bell, W. L. Meyer and B. T. Zinn, "Predicting the Acoustics of Arbitrarily Shaped Bodies Using an Integral Approach," AIAA J., Vol. 15(6), 813-820, 1977.

19. G. H. Koopman and H. Benner, "Method for Computing the Sound Power of Machines Based on the Helmholtz Integral," J. Acoust. Soc. Am., Vol. 71(1), 78-89, 1982.

20. A. F. Seybert, B. Soenarko, F. J. Rizzo, and D. J. Shippy, "Application of the BIE Method to Sound Radiation Problems Using an Isoparametric Element," ASME J. Vib. Acoust. Stress Rel. Dsgn., Vol. 106(3), 414-420, 1984.

21. A. F. Seybert, B. Soenarko, F. J. Rizzo, and D. J. Shippy, "An Advanced Computational Method for Radiation and Scattering of Acoustic Waves in Three Dimensions," J. Acoust.Soc. Am.. Vol. 77(2), 362-368, 1985.

22. A. F. Seybert, B. Soenarko, F. J. Rizzo, and D. J. Shippy, "A Special Integral Equation Formulation for Acoustic Radiation and Scattering for Axisymmetric Bodies and Boundary Conditions," J. Acoust. Soc. Am., Vol. 80(4), 1241-1247, 1986.

23. B. B. Baker and E. T. Copson, The Mathematical Theory of Huygen's Principle, Oxford, London, 1939.

24. L. H. Chen and D. G. Schweikert, "Sound Radiation from an Arbitrary Body," J. Acoust. Soc. Am., Vol. 35(10), 1626-1632, 1963.

25. P. J. T. Filippi, "Layer Potentials and Acoustic Diffraction," J. Sound Vib., Vol. 54(4), 473-500, 1977.

26. C. A. Brebbia, The Boundary Element Method for Engineers, John Wiley & Sons, New York, 1978.

27. C. A. Brebbia and S. Walker, "Boundary Element Techniques in Engineering," Newness - Butterworths, 1980.

28. C. A. Brebbia, J. Telles and L. Wrobel, Boundary Element Techniques: Theory and Applications in Engineering, Springer-Verlag, New York, 1984.

29. P. K. Banerjee and R. Butterfield, Boundary Element Methods in Engineering Science, McGraw-Hill, New York, 1981.

30. R. P. Shaw, "Boundary Integral Equation Methods Applied to Wave Problems," in Developments in Boundary Element Method I, Banerjee, Butterfield, eds, Applied Science Publishers, London, Chapter 6, 1979.

31. H. Huang, "Helmholtz Integral Equations for Fluid-Structure Interaction," Advances in Fluid-Structure Interaction, ASME, New York, AMD Vol. 64, 19-38, 1984.

32. A. F. Seybert and T. K. Rengarajan, "The Use of CHIEF to Obtain Unique Solutions for Acoustic Radiation Using Boundary Integral Equations," J. Acoust. Soc. Am., Vol. 81(5), 1299-1306, 1987.

33. P. M. Morse and H. Feshbach, Methods of Theoretical Physics, Part I, Chapter 7, McGraw-Hill, New York, 1953.

34. B. Soenarko, "An advanced Boundary Element Formulation for Acoustic Radiation and Scattering in Three Dimensions," Ph. D. dissertation, Department of Mechanical Engineering, University of Kentucky, 1983.

35. A. F. Seybert, C. Y. R. Cheng, "Application of the Boundary Element Method to Acoustic Cavity Response and Muffler Analysis," ASME Transactions, J. Vib. Acoust. Stress and Rel. in Design, Vol. 109, 15-21, 1987.

36. H. A. Schenck and G. W. Benthien, "The Application of a Coupled Finite-Element Boundary-Element Technique to Large-Scale Structural Problems," Advances in Boundary Elements: Vol. 2, edited by C. A. Brebbia and J. J. Connor, Computational Mechanics Publications, Southampton, 309-319, 1989.

37. T. W. Wu, A. F. Seybert and G. C. Wan, "Vectorization and Parallelization of the Acoustic Boundary Element Code BEMAP on the IBM ES/3090 VF," Proceeding of International Congress on Recent Developments in Air- and Structural-Borne Sound and Vibration, 489-498, March 6-8, 1990, Auburn University, U.S.A..

38. A. F. Seybert, T. W. Wu, X. F. Wu, and F. B. Oswald, "Acoustical Analysis of Gear Housing Vibration", *NASA TM 103691*, 1991.

39. A. F. Seybert, R. Khurana, "Calculation of the Sound Intensity and Sound Radiation Efficiency of a Structure from Vibration Data," Proceedings, International Modal Analysis Conference, 302-308, February 1-4, 1988.

40. A. F. Seybert, T. W. Wu and W. L. Li, "Acoustical Prediction for Structural Radiation and Propagation in Automotive Applications," Proceedings, 1989 SAE Noise and Vibration Conference, Traverse City, Michigan, 427-436, May 16-18, 1989.

41. A. F. Seybert, C. Y. R. Cheng, "Application of the Boundary Element Method to Acoustic Cavity Response and Muffler Analysis," ASME Transactions, J. Vib. Acoust. Stress and Rel. in Design., Vol. 109, 15-21, 1987.

42. C. Y. R. Cheng, A. F. Seybert and S. G. Liu, "Acoustic Resonator Analysis Using the Boundary Element Method for Application to Air-Handling System Design," ASHRAE Transactions, Vol. 95, Part 1, 76-82, 1989.

43. A. F. Seybert, T. W. Wu and G. C. Wan, BEMAP USER'S MANUAL, Version 2.43, Department of Mechanical Engineering, University of Kentucky, 1990.

44. C. E. Wallace, "The Radiation Efficiency of Rectangular Panels," J. Acoust. Soc. Am., Vol. 51(3). Part 2, 946-952, 1972.

45. J. Y. Chung, "Cross-Spectral Method of Measuring Acoustic Intensity Without Error Caused by Instrument Phase Mismatch," J. Acoust. Soc. Am., Vol. 64(6), 1613-1616, 1978.

46. F. J. Fahy, " Measurement of Acoustic Intensity Using the Cross-Spectral Density of Two Microphone Signals," J. Acoust. Soc. Am., Vol. 62(4), 1057-1059, 1977.

47. Computational Systems, Inc., RT Intensity User's Manual, 1988.

48 A. W. Leissa, Vibration of Plates, NASA SP-160, 1969.

49. G. Maidanik, "Response of ribbed panels to reverberant fields," J. Acoust. Soc. Am. , Vol. 34(6), 809-826, 1962.

50. F. Fahy, Sound and Structural Vibration, Radiation, Transmission and Response, Academic Press, 1985.

51. L. E. Kinsler, A. R. Frey, A. B. Coppens, and J. V. Sanders, Fundamentals of Acoustics, third edition, 1982.

REPORT DOCUMENTATION PAGE

Form Approved
OMB No. 0704-0188

Public reporting burden for this collection of information is estimated to average 1 hour per response, including the time for reviewing instructions, searching existing data sources, gathering and maintaining the data needed, and completing and reviewing the collection of information. Send comments regarding this burden estimate or any other aspect of this collection of information, including suggestions for reducing this burden, to Washington Headquarters Services, Directorate for Information Operations and Reports, 1215 Jefferson Davis Highway, Suite 1204, Arlington, VA 22202-4302, and to the Office of Management and Budget, Paperwork Reduction Project (0704-0188), Washington, DC 20503.

1. AGENCY USE ONLY (*Leave blank*)	2. REPORT DATE	3. REPORT TYPE AND DATES COVERED
	January 1994	Final Contractor Report

4. TITLE AND SUBTITLE

Experimental Validation of Finite Element and Boundary Element Methods for Predicting Structural Vibration and Radiated Noise

5. FUNDING NUMBERS

WU–505–62–10
1L162211A47A
G–NAG3–912

6. AUTHOR(S)

A.F. Seybert, T.W. Wu, and X.F. Wu

7. PERFORMING ORGANIZATION NAME(S) AND ADDRESS(ES)

University of Kentucky
Lexington, Kentucky 40506–0046

8. PERFORMING ORGANIZATION REPORT NUMBER

E–8264

9. SPONSORING/MONITORING AGENCY NAME(S) AND ADDRESS(ES)

Vehicle Propulsion Directorate
U.S. Army Research Laboratory
Cleveland, Ohio 44135–3191
and
NASA Lewis Research Center
Cleveland, Ohio 44135–3191

10. SPONSORING/MONITORING AGENCY REPORT NUMBER

NASA CR–4561
ARL–CR–109

11. SUPPLEMENTARY NOTES

Project Manager, Fred B. Oswald, Propulsion Systems Division, NASA Lewis Research Center, (216) 433–3957.

12a. DISTRIBUTION/AVAILABILITY STATEMENT

Unclassified - Unlimited
Subject Category 37

12b. DISTRIBUTION CODE

13. ABSTRACT (*Maximum 200 words*)

This research report is presented in three parts. In the first part, acoustical analyses were performed on modes of vibration of the housing of a transmission of a gear test rig developed by NASA. The modes of vibration of the transmission housing were measured using experimental modal analysis. The boundary element method (BEM) was used to calculate the sound pressure and sound intensity on the surface of the housing, and the radiation efficiency of each mode. The radiation efficiency of each of the transmission housing modes was then compared to theoretical results for a finite baffled plate. In the second part, analytical and experimental validation of methods to predict structural vibration and radiated noise are presented. A rectangular box excited by a mechanical shaker was used as a vibrating structure. Combined finite element method (FEM) and boundary element method (BEM) models of the apparatus were used to predict the noise level radiated from the box. The FEM was used to predict the vibration, while the BEM was used to predict the sound intensity and total radiated sound power using surface vibration as the input data. Vibration predicted by the FEM model was validated by experimental modal analysis, noise predicted by the BEM was validated by measurements of sound intensity. Three types of results are presented for the total radiated sound power: (1) sound power predicted by the BEM model using vibration data measured on the surface of the box; (2) sound power predicted by the FEM/BEM model; and (3) sound power measured by an acoustic intensity scan. In the third part, the structure used in part two was modified. A rib was attached to the top plate of the structure. The FEM and BEM were then used to predict structural vibration and radiated noise respectively. The predicted vibration and radiated noise were then validated through experimentation.

14. SUBJECT TERMS

Boundary element method; Finite element method; Acoustic intensity method; Noise; Vibration; Vibration modes

15. NUMBER OF PAGES
105

16. PRICE CODE
A06

17. SECURITY CLASSIFICATION OF REPORT	18. SECURITY CLASSIFICATION OF THIS PAGE	19. SECURITY CLASSIFICATION OF ABSTRACT	20. LIMITATION OF ABSTRACT
Unclassified	Unclassified		

National Aeronautics and
Space Administration
Code JTT
Washington, D.C. 20546-0001

Official Business
Penalty for Private Use $300

POSTMASTER: If Undeliverable — Do Not Return